

TWO *IN VIVO* METHODS FOR DETERMINING
FLUORINE CONTENT IN BONE

**ANALYSIS AND
MODIFICATIONS OF TWO
IN VIVO METHODS FOR
DETERMINING FLUORINE
CONTENT IN BONE**

by

MONIQUE STUIVE , B.SC.

Thesis Submitted in Partial Fulfillment of the
Requirements for the Degree of
Master of Science

in the
Radiation Sciences Program
Faculty of Science

© Monique Stuiwe 2018
MCMASTER UNIVERSITY
Summer 2018

TITLE: Analysis and modifications of two *in vivo* methods for determining fluorine content in bone

AUTHOR: Monique Stuive, B.Sc.

SUPERVISOR: Dr. Fiona McNeill

NUMBER OF PAGES: xv, 117

DEGREE: Master of Science, Radiation Sciences Program, 2018

SCHOOL: McMaster University, Hamilton, Ontario

Lay Abstract

Fluorine is an element which accumulates in bones and teeth. High levels of fluorine have been shown to be unhealthy, causing both dental and skeletal fluorosis. Low levels of fluorine have been shown to reduce dental cavities, however, their effect on bone health is not well understood. Currently, fluorine can be measured in bone samples from either biopsies or cadavers. Having a non-invasive way to measure fluorine concentrations in living humans without the need for surgery would be invaluable. These measurements could be used to optimize treatment for osteoporosis patients or to determine if emergency measures are necessary in cases of high accidental doses to members of the public. Additionally, long-term studies examining fluorine metabolism and bone health could be performed on population groups of interest. For these reasons, two different non-invasive methods for determining fluorine content in bone were analyzed and enhancements to each measurement technique attempted.

Abstract

Non-invasive techniques to measure bone fluorine levels *in vivo* are few and not well studied. These techniques would prove useful for longitudinal studies of fluorine accumulation and treatment optimization for patients with poor bone health. Two measurement techniques were analyzed and improvements to each technique attempted with bone samples and bone-mimicking phantoms. The first method analyzed was neutron activation analysis (NAA), a technique previously studied in our laboratory. A previous detector setup consisting of nine sodium iodide detectors was re-tested and a new detector setup consisting of two high-purity germanium detectors was also tested. The detection limit of the sodium iodide setup was found to be higher than previously reported by a factor of 4, and the new high-purity germanium detector setup was found to result in a higher detection limit by a factor of 5 compared to the sodium iodide setup. The second method analyzed was nuclear magnetic resonance (NMR). Magic angle spinning was performed on a human bone sample, and a novel probe was constructed for future *in vivo* measurements. MAS NMR measurement of the human bone sample showed it to have an appropriate chemical shift and shape consistent with previous research on substances similar to bone. The constructed probe successfully resonated at the appropriate frequency, however there were potential contamination problems which prevented a measurable fluorine signal from being obtained. Both the NAA and NMR techniques may be optimized further, though with the results obtained, NAA remains the more sensitive technique for measuring bone fluorine *in vivo*.

Keywords: Fluorine; Bone; Neutron Activation Analysis; High-purity Germanium (HPGe); Trace Element Detection; Nuclear Magnetic Resonance

Acknowledgements

Thanks to supervisor Fiona McNeill, committee members David Chettle and Mike Noseworthy, and others who helped collect experimental data including: Justin Bennett, Bob Berno, Mike Inskip, Sergey Krachkovskiy, Alice Pidruczny, and Bill Prestwich.

Table of Contents

Descriptive Note	ii
Lay Abstract	iii
Abstract	iv
Acknowledgements	vi
Table of Contents	vii
List of Tables	ix
List of Figures	x
List of Abbreviations	xiv
Declaration of Academic Achievement	xv
1 Introduction	1
2 Neutron Activation Analysis Experiments	10
2.1 NAA Background	10
2.1.1 Origin of the Signal	10
2.1.2 Gamma-ray Detection	13
2.2 Previous Work	14
2.3 Methods	19
2.3.1 Hand Simulating Phantom	19
2.3.2 Experimental Detector Setup	21

2.3.3	Irradiation Protocol	27
2.3.4	Calculating a Minimum Detection Limit	28
2.4	Results	45
2.5	Discussion	50
3	Nuclear Magnetic Resonance Experiments	58
3.1	NMR Background	58
3.1.1	Origin of the Signal	58
3.1.2	Parameters Affecting the Signal	61
3.1.3	General Probe Design	64
3.1.4	Fluorine NMR of Bone	66
3.2	Methods	70
3.2.1	MAS Experiment	70
3.2.2	Bulk Sample Experiment	73
3.3	Results	78
3.3.1	MAS Experiment	78
3.3.2	Bulk Sample Experiment	81
3.4	Discussion	82
4	Conclusion	90
	Bibliography	94

List of Tables

Table 2.1	Elemental composition of the hand simulating phantoms, as well as the radionuclides produced following neutron activation and their associated half-lives and daughter gamma-ray energies.	21
Table 2.2	Basic properties of the two HPGe detectors used in the experimental work.	25
Table 2.3	HPGe detector performance metrics including: FWHM, Peak-to-Compton ratio, absolute detection efficiency with a source to detector difference of 25 cm, and relative efficiency compared to a 3" by 3" NaI(Tl) detector.	46
Table 2.4	Comparison between previously determined MDL values and current experimental MDL values using 30 s measurement times for the NaI(Tl) system and 150 s measurement times for the HPGe system.	53
Table 3.1	Heating temperatures and holding times in oven to allow ashing of bone pieces. Ashing was done to make the sample more stable and compact when performing MAS.	72
Table 3.2	Final input values to the birdcage builder app resulting in capacitance values that agreed with experimental findings.	77
Table 3.3	Comparison of approximate detection amounts of various experiments performing fluorine detection in bone or representative materials. *based on proton frequencies	86

List of Figures

Figure 1.1	The possible relationships between fluoridation level and relative bone health. Knowledge of the fluoridation levels corresponding to both maximum bone health and decreased bone health would be useful for determining proper intake amounts.	4
Figure 2.1	4π NaI(Tl) detection system responses in three different modes to a bone phantom containing 256 mg F that was neutron activated and subsequently measured. The three different modes tested were: anti-coincidence mode (a), coincidence mode (b), and singles mode (c). Chlorine-38's cascade gamma rays result in the peaks seen in (b) at 1642.4 keV and 2167.5 keV. The main peak between 1600 and 1700 keV in (c) is composed of both the fluorine-20 peak at 1633.6 keV and the chlorine-38 peak at 1642.4 keV. The lower energy peak to the left of this peak is a result of the potassium-40 peak at 1460.8 keV and the sodium-24 peak at 1368.6 keV.	24
Figure 2.2	Energy resolution of HPGe Detector 1 to cobalt-60's 1332.5 peak before (a) and after (b) annealing. The FWHM was reduced by 4.0 keV, bringing it to a value of 3.0 keV, which is still sub-optimal but adequate to resolve the fluorine-20 and chlorine-38 peaks.	26

Figure 2.3	Experimental setup of HPGe Detector 1 (left) and HPGe Detector 2 (right) including borated concrete, lead, borated rubber sheets, and wax for shielding of both gamma rays and neutrons.	27
Figure 2.4	Detector response function of HPGe Detector 1 (a) and HPGe Detector 2 (b) to the 1332.5 keV peak of Co-60. . .	46
Figure 2.5	Measurement spectra collected on HPGe Detector 1 for 30 s following neutron irradiation and a 15 s transfer time of: a 256 mg F phantom (a), no phantom (b), and the same 256 mg F phantom displayed in a smaller energy region corresponding to the fluorine-20 peak (c). . .	47
Figure 2.6	Measurement spectra collected on HPGe Detector 2 for 30 s following neutron irradiation and a 15 s transfer time of: a 256 mg F phantom (a), no phantom (b), and the same 256 mg F phantom displayed in a smaller energy region corresponding to the fluorine-20 peak (c). . .	48
Figure 2.7	Measurement spectra collected on the NaI(Tl) system for 30 s following neutron irradiation and a 15 s transfer time of: a 256 mg F phantom (a), no phantom (b), and the same 256 mg F phantom displayed in a smaller energy region corresponding to the fluorine-20 peak (c). . .	49
Figure 2.8	Calibration line determining the relationship between the experimental F/Ca peak ratios and associated errors to the known concentrations of the phantom in mg F/g Ca for HPGe Detector 1 ($\chi^2 = 8.0$).	50
Figure 2.9	Calibration line determining the relationship between the experimental F/Ca peak ratios and associated errors to the known concentrations of the phantom in mg F/g Ca for HPGe Detector 2 ($\chi^2 = 6.5$).	51

Figure 2.10	Calibration line determining the relationship between the experimental F/Ca peak ratios and associated errors to the known concentrations of the phantom in mg F/g Ca for the NaI(Tl) detection system ($\chi^2 = 2.6$). . .	52
Figure 3.1	Comparison of bone samples with different processing procedures. The ashed bone powder (a) was more stable than the crushed bone pieces (b) and able to spin at higher frequencies.	72
Figure 3.2	Pulse program used in Topspin to excite the bone sample and collect the FID. One 90° pulse was applied as well as two 180° refocussing pulses. The FID was then recorded. There was a 1.5 s relaxation delay between the end of data collection for an applied pulse and the start of a new excitation pulse.	74
Figure 3.3	Birdcage builder app interface used to determine the required capacitance for each capacitor on the birdcage legs. Input values were estimated from the physical probe design.	76
Figure 3.4	Prototype coil for measurement of bulk bone samples containing fluorine. The coil is shown with connections made to the probe body.	77
Figure 3.5	Resonant peaks of the prototype coil as displayed on a spectrum analyzer. The first peak corresponds to the desired resonant frequency of 188 MHz. The number of resonant peaks depends on the number of legs in the birdcage coil.	78

Figure 3.6	Experimental setup for testing of the prototype coil. The probe body used to make the measurements is displayed in (a), where the prototype coil can be seen attached on top. The matching and tuning adjustments are made with rods at the bottom of the probe body. The metal body provides shielding. The 200 MHz spectrometer that was used to perform testing is displayed in (b). . . .	79
Figure 3.7	Spectrum of a 0.05 g fluoridated hydroxyapatite sample collected from a 11 kHz MAS experiment with 256 repetitions.	80
Figure 3.8	Spectrum of a 0.1 g ashed bone sample collected from a 11 kHz MAS experiment with 8192 repetitions.	80
Figure 3.9	Fit to the ashed bone spectrum shown in Figure 3.8. The fit shows the placement of the spinning sidebands and the uneven distribution of signal intensity in the sidebands.	81
Figure 3.10	Comparison of chemical shift between the fluoridated hydroxyapatite spectrum and the ashed bone spectrum. The ashed bone spectrum has a more negative chemical shift. The sideband intensity pattern is similar in both spectra.	82

List of Abbreviations

BMD	Bone Mineral Density.
CSA	Chemical Shift Anisotropy.
FID	Free Induction Decay.
FWHM	Full Width Half Maximum.
HPGe	High Purity Germanium.
ICRP	International Commission on Radiological Protection.
IVWM	Inverse Variance Weighted Method.
MAS	Magic Angle Spinning.
MDL	Minimum Detection Limit.
MRI	Magnetic Resonance Imaging.
NAA	Neutron Activation Analysis.
NaI(Tl)	Sodium Iodide doped with Thallium.
NMR	Nuclear Magnetic Resonance.
PIGE	Proton Induced Gamma Emission.
ppm	parts per million.
QSM	Quantitative Susceptibility Mapping.

Declaration of Academic Achievement

This thesis represents original research that I, Monique Stuive, conducted. My supervisor, Fiona McNeill, and the members of my supervisory committee, David Chettle and Michael Noseworthy, provided guidance. I completed all experimental work and wrote all sections of the written document. To the best of my knowledge, the content of this document does not infringe on anyone's copyright. Bob Berno (McMaster NMR Facility) helped set up the Magic Angle Spinning experiments and collect data. Sergey Krachkovskiy (McMaster Chemistry Department) gave useful information and helped design the bulk sample probe.

Chapter 1

Introduction

Extremely reactive, the most electronegative atom, found in 20–25% of pharmaceuticals [1, 2], the thirteenth most abundant element in both the human body and in the Earth's crust by weight [3], fluorine (F) is an element worthy of study. Even a single fluorine atom in a molecule can have a great effect on the physical and chemical properties of the compound [4]. In fact, fluorine is better known as fluoride, the name given to it when found in a compound or as an anion as it is almost always bonded and rarely found in elemental form.

Fluorine is present in food and water in variable amounts according to geographical location and water supply treatment. Spatial distribution of

naturally high fluoride levels is primarily determined by geology, climate, and topography [5]. Industrial sources of fluorine into the environment include: coal burning, oil refining, steel production, brick-making, and phosphatic fertilizer plants [6]. Specifically for humans, fluoridation of municipal drinking waters and certain lifestyle habits such as tea-drinking [7] affect the amount of fluorine ingested by individuals. Thus, levels in humans are highly variable, where the estimated daily intake of fluoride is between 0.3–1.8 mg for an adult [8].

Apatite is a mineral group that can be found in biological systems as it makes up the crystal structure of bones and teeth. Due to the capability of apatite to form bonds with a variety of compounds, bone serves a potential indicator of environmental exposure for these compounds. Bone's absorbency of compounds is so high that bone char is used to remove contaminants from water [9,10]. The apatite in bone is often referred to as hydroxyapatite ($\text{Ca}_5(\text{PO}_4)_3(\text{OH})$), however bone apatite is highly substituted and contains only 20% of the hydroxyl ions which would be expected if it was pure calcium hydroxyapatite [11]. Fluorine is one such compound that accumulates in the human body through bonding to the apatite component of bones and teeth. It is absorbed from the gastrointestinal tract into body fluids and either cleared through urinary excretion or absorbed into the

apatite matrix. At lower intakes, 50–57% of ingested or inhaled fluorine is bound to the skeleton, where clearance takes over four times longer than uptake [12]. Bones and teeth contain 99% of the fluoride body burden as soft tissues do not accumulate fluoride [13], and the blood-brain barrier limits diffusion of fluoride into the central nervous system [14].

Due to the strong bonds it forms, fluorine is often added to materials for structural stability. It is for this reason that fluorine is found in toothpastes and drinking water. At low levels, fluoride confers a protective effect on teeth by significantly reducing the number of dental caries [15]. It is possible that low levels of fluorine could have beneficial effects on bone health, conferring strength and a lower level of fracture rates. However, at high levels, it has a detrimental effect on the health of bones and teeth in the form of skeletal and dental fluorosis [16]. The effect of different fluorine levels on bone health is a question that is currently under investigation, as data on low doses of fluoride remain inconclusive. Figure 1.1 outlines possible bone health trends with increasing fluoridation.

Large historical studies have had conflicting results. A study of osteoporosis patients treated with sodium fluoride found increased bone volume and trabecular thickness, increased osteoid accumulation, and no

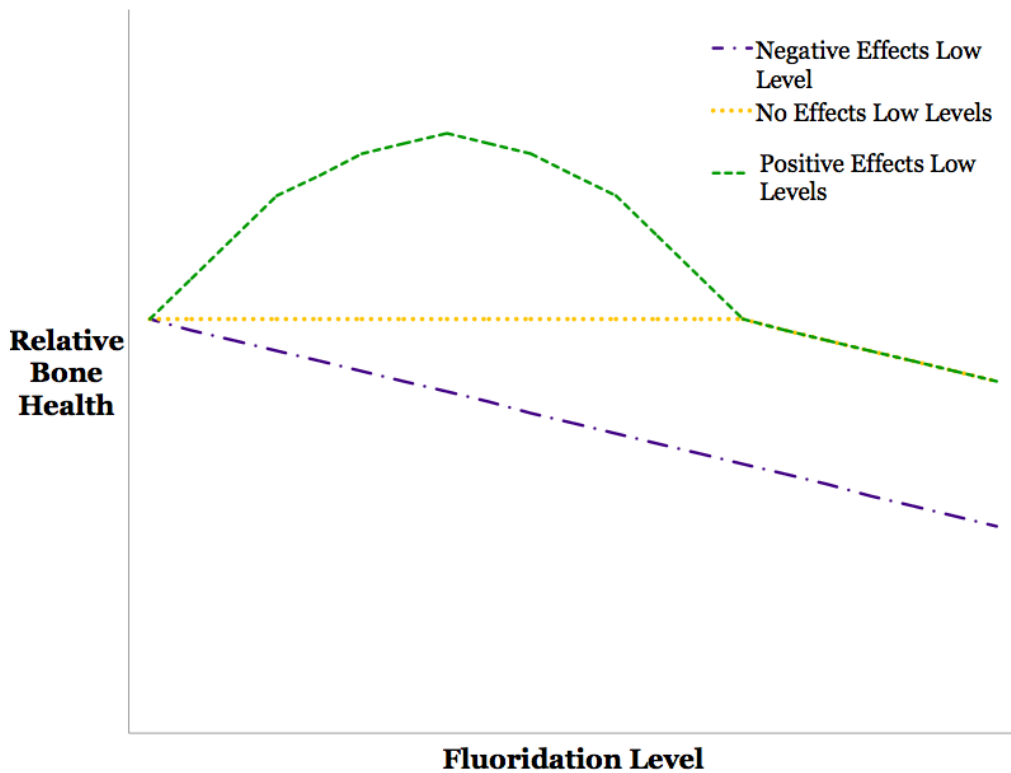


Figure 1.1: The possible relationships between fluoridation level and relative bone health. Knowledge of the fluoridation levels corresponding to both maximum bone health and decreased bone health would be useful for determining proper intake amounts.

difference in bone formation [17]. A cell culture study found that fluoride actually stimulated bone formation, but impaired mineralization at high doses [18]. An animal study investigating the impact of increased sodium fluoride found that bone turnover was increased, bone volume unchanged, and cancellous bone strength reduced [19]. Another study found that a low fluoride dose was associated with a reduction in fracture risk, and fluoride

treatment increased bone mineral density depending on treatment duration [20].

In studies comparing fluoridated and non-fluoridated communities, there have been no reported differences in bone mineral density [21–23] while fracture incidence as a result of fluoridation has been reported to both decrease [22] and not be affected [23]. One study determined that to answer properly the question of fracture rate incidence due to drinking water fluoridation, a sample size of greater than 400,000 subjects would be required due to the many confounding variables [24].

Recent research is still divided regarding fluoride's beneficial effect on bone. Some reports found negative effects including insulin resistance, increased concentrations of tumor necrosis factor, decreased trabecular bone area of the tibia [25], and a reduction in trabecular bone volume and fracture load [26]. Others found mixed results including no correlation with bone density or bone mineral concentration [27,28]. Still, others found positive results including improvements in bone microarchitecture and higher Ca content [29], dose dependent enhanced bone mineralization [30], and increases in mandibular bone volume and trabecular thickness [31].

Due to the large variation in research subjects, meta-analyses on the subject have mostly concluded that fluoride's influence on bone metabolism is poorly defined. Fluorine leads to a diverse collection of responses, has a narrow therapeutic/toxicity window, and deeper investigations are required including analyzing the role of an individual's genetic background [32,33].

Fluorine does not just affect bone by adding structural support to the hydroxyapatite matrix. It has also been shown to have effects on osteoclast proliferation, differentiation and resorption [34,35], genes associated with oxidative stress, inflammation, osteoblastic differentiation, bone development pathways in osteosarcoma cells [36], pathways related to connective tissue formation, bio-mineral tissue development, endochondral bone formation, bone and skeletal morphogenesis [37], genes involved in osteogenesis, IGF-1 [38], alkaline phosphatase [39], bone mineral metabolism and extracellular matrix formation [40], and the expression of osteoprotegerin in osteoblast-like cells [41].

Due to its diverse effects and controversial effect on bone health, elucidating the ideal range of fluoride levels *in vivo* through comparison studies of various exposure effects may be useful in mitigating current health risk to humans. Knowing the ideal amount of bone fluoride is useful to

counteract osteoporosis and in the synthesis of apatite coatings for bone allograft implants with better osseo-integration, as even small substitutions can have large effects on performance [42] .

To determine the effects of fluoride, accurate measurement techniques are necessary. Development of an easy, safe method for the analysis of fluorine is challenging, especially for solid materials like bone. Methods using aqueous solutions involve laborious and potentially hazardous sample preparation procedures in order to remove the fluorine from the solid and get it in solution. An ion electrode has been used in a previous study to measure fluorine concentration and found mass concentrations of 610 parts per million (ppm) in dry weight, 1100 ppm in ash weight in the human rib, and mass concentrations of 530 ppm in dry weight, 960 ppm in ash weight in a human iliac crest [43]. Proton Induced Gamma Emission (PIGE) is another technique which has been used to determine fluorine content. Fluorine levels were found to be $1,659 \pm 792$ mg/kg dry mass of human rib bone (soft tissues and blood removed, freeze-dried, and heated at 110°C for 92 hrs) [44]. Other PIGE studies found 500–1999 μgg^{-1} [45] and 435 μgg^{-1} [46]. These techniques are not possible *in vivo* due to the sample preparation requirements.

Having a way to measure fluorine concentrations in humans non-invasively is valuable. These measurements could be used to optimize treatment for osteoporosis patients or to determine if emergency measures are necessary in cases of high accidental doses. As well, longitudinal studies may be performed without painful bone biopsies to examine the effects of different factors on fluoride metabolism. Difference measurements could be made to determine fluorine content before and after an activity or intervention. Anthropological studies may be performed, and at-risk populations possibly identified. Furthermore, knowledge of how fluorine interacts in bone provides insight into the metabolism of other elements in bone. For these reasons, the current state of two different methods for *in vivo* fluoride measurement was analyzed, and enhancements to each measurement technique attempted. Further refinement of the detection methodology and the experimental design could result in enhanced sensitivity and a lowered detection limit. Improving the accuracy of this diagnostic tool would be useful in determining the variables which contribute to fluoride uptake and retention.

Chapter 2 details the first method of Neutron Activation Analysis (NAA) and describes the work performed analyzing two different detector setups. Chapter 3 details the second method of Nuclear Magnetic Resonance (NMR) and describes the work performed, processing and testing an

anatomical bone sample using a specialized technique as well as the design of a prototype *in vivo* probe.

Chapter 2

Neutron Activation Analysis

Experiments

2.1 NAA Background

2.1.1 Origin of the Signal

Neutron activation is a technique which uses neutrons to render specific nuclei in a sample unstable for the purpose of elemental analysis. The produced unstable nuclei will undergo radioactive decay, a process which may result in the emission of a gamma ray at a specific energy which may be

detected by nearby detectors. Identification and quantification of gamma-ray emitting radionuclides via gamma-ray spectroscopy immediately following neutron activation is a technique known and described as neutron activation analysis (NAA). The atomic number of the target nucleus, determined by the number of protons, remains constant while the mass number, determined by the sum of the number of protons and neutrons, increases. This results in a new isotope of the starting element. If this isotope is unstable, it is called "activated", as it will decay by giving off radiation and has now earned the title of "radionuclide". Most radionuclides produced by neutron bombardment are beta-active with a wide range of half-lives. In beta-minus decay, one neutron is converted to a proton and an electron (or beta minus) particle. The electron, as well as an electron antineutrino, are ejected from the nucleus. Beta decays often populate an excited state of the product daughter nucleus so that subsequent de-excitation gamma rays are emitted essentially together with the beta particles.

Fluorine-19 is the only naturally occurring stable isotope of fluorine, and will turn into the radioisotope fluorine-20 upon absorption of a neutron. Fluorine-20 has a half-life of 11.163 s and decays through beta-minus decay to an excited state of neon-20 that is de-excited via emission of a gamma ray at 1633.6 keV 99.1% of the time [47]. Thus, a mass of natural fluorine

exposed to a neutron field of the appropriate energy will result in an amount of ^{20}F with a certain activity. The activity (A) of a daughter radionuclide from the irradiation of a mass of an element (m) in a neutron field can be determined from

$$A = K(1 - e^{-\lambda t}), \quad (2.1)$$

where t is the length of time in the neutron field, and λ is the decay constant of the nuclide produced. K is given by

$$K = \theta \frac{m}{M} N_A \int \phi(E) \sigma(E) dE, \quad (2.2)$$

where θ is the isotopic abundance of the relevant isotope in the natural form of the element being measured, m is the mass, M is the molar mass, N_A is Avogadro's number, $\phi(E)$ is the neutron energy fluence spectrum, and $\sigma(E)$ is the neutron capture cross-section as a function of neutron energy.

2.1.2 Gamma-ray Detection

The first step of NAA is to induce radioactivity in the sample. The second step of NAA is to determine the starting concentration of the element of interest in the target sample via subsequent detection and quantification of the intensities and energies of the emitted radiation. Alpha particles, beta particles, and gamma rays can all be emitted following neutron activation. However, detection is usually limited to gamma rays due to the limited range of charged particles. For a radiation detector to record a pulse, the gamma ray must interact within the active volume of the radiation detector, leading to the creation of a charge pulse that is collected through the application of a voltage. The total charge is recorded as this is proportional to the amount of energy deposited into the detector volume. The charge can be created directly in a solid state detector where ionizing radiation generates pairs of charge carriers. In scintillation detectors, the charge is created indirectly where ionizing radiation results in luminescence. In a connected photo-multiplier tube, this luminescence is converted to charge at the photocathode, and this charge is multiplied through a dynode chain.

In a perfect detector, every gamma ray passing through the active volume would be turned into a pulse exactly corresponding to its energy.

However, in physical detectors, there is a probability that a gamma ray will escape or deposit only a fraction of its energy. As well, there are fluctuations in the energy response of physical detectors to incident gamma rays. These fluctuations are due to random noise and drift within the detector as well as statistical fluctuations in the number of produced information carriers. Thus, the two main factors taken into account when comparing gamma-ray spectroscopy units are the efficiency (the number of counts recorded compared to the number of decay gamma rays emitted) and the energy resolution (the spread in the range of energies recorded for an incident gamma ray of a specific energy). Intuitively, one desires a high efficiency and a high energy resolution.

2.2 Previous Work

For neutron activation to occur, a source for the neutron energy fluence spectrum in Equation 2.2 is required. Intense, controllable neutron fields are a precious resource typically requiring a nuclear reactor or particle accelerator. At McMaster University, there is a tandem accelerator that acts as a neutron source for neutron activation analysis. This accelerator works by boiling off electrons in a filament which are then bound to a hydrogen

source gas. This gas of negatively charged hydrogen ions is contained by magnets. When a beam is required, an anode pushes out the negatively charged hydrogen gas which is then accelerated towards a positively charged high-voltage terminal, gaining energy. This terminal contains a stripping gas which will remove both electrons from the negatively charged hydrogen ion. Now repelled by the positive terminal, the beam of protons is repelled away, gaining more energy. Due to the fact that the protons gain double the energy of the voltage applied, the accelerator is called a tandem accelerator. After gaining energy, the beam is focussed with magnets until it hits a target. To produce neutrons, this target is composed of lithium as neutrons will be produced by the ${}^7\text{Li}(p,n){}^7\text{Be}$ reaction, so long as protons have an energy greater than the energy threshold of 1.88 MeV.

Part of the laboratory setup includes a hand irradiation system. This system is a self-enclosed cavity except for an access port to allow research participants to insert their hand during experiments. When testing with phantoms, there is a plug where a human arm would be to minimize radiation escaping the box. To maximize the probability of neutron interaction, there are polyethylene walls to moderate the neutrons down to slower energies and a graphite reflector to re-direct neutrons that did not interact during the first pass-through. To minimize the dose during

irradiation, there are borated plastic sheets to attenuate neutrons, a lead filter to reduce hand dose from gamma rays within the target, and outer lead walls to attenuate gamma radiation from exiting the target space. The system has been described in detail previously in Ref. [48].

The Tandem Accelerator Laboratory at McMaster University has been the site of several trace element detection setups using neutron activation analysis including aluminum [49, 50], manganese [51–53], and fluorine [54–56]. Each element comes with its own unique set of properties and limitations. For example, there is more fluorine in the body than aluminum, however the half-life of fluorine-20 is much shorter at only 11 s compared to aluminum-28's half-life of 135 s. The work done in this laboratory is the only research examining neutron activation as a way to measure fluorine levels *in vivo*. The lowest published detection limit recorded for fluorine is 0.17 mg fluorine/g calcium [55].

In this method, calibration phantoms were irradiated in the tandem accelerator and subsequently measured on a 4π sodium iodide doped with thallium NaI(Tl) system. This system consists of nine NaI(Tl) detectors arranged in a geometry providing almost 4π coverage. The characteristics

and specifications of this detector setup have been described before in Refs [57, 58].

The NaI(Tl) detectors can be operated at room temperature. However, fluctuations in atmospheric conditions can cause gain variations between detectors in a multi-detector system which may negatively impact the overall energy resolution. These detectors also suffer from poor resolution due to the statistical spread in the number of photoelectrons created in the photomultiplier tube. The sensitivity of the detection system is inversely related to the square root of the resolution [59]. Improvement to the NAA technique as evidenced by a lower detection limit might come from the use of semiconductor detectors instead of NaI(Tl) detectors due to the significantly better energy resolution of the former. As well, while using the NaI(Tl) detectors, there is interference between the ^{20}F and ^{38}Cl gamma rays in the spectrum, and the ^{38}Cl signal must be subtracted to obtain the fluoride concentration. This increases measurement uncertainty and makes the detection limit poorer. Semiconductor detectors clearly resolve the two signals, avoiding the need for subtraction.

The resolution of the detector determines the width of peaks in a collected energy spectrum, and values for the resolution are typically quoted

as the full width at half maximum (FWHM), or peak width (W_T). A common semiconductor detector type used for gamma-ray detection is a high-purity germanium detector (HPGe). This type of detector is also referred to as a hyperpure germanium detector, or simply, a germanium detector. The resolution of a high-purity germanium detector is determined by

$$W_T^2 = W_D^2 + W_X^2 + W_E^2, \quad (2.3)$$

where W_D^2 is the peak width contribution from carrier statistics, W_X^2 is the peak width contribution from incomplete charge carrier collection, and W_E^2 is the peak width contribution from electronic noise [60]. The limit on the resolution of a high-purity germanium (HPGe), detector is given by [60]

$$W_D^2 = (2.35)^2 F \epsilon E, \quad (2.4)$$

where F is the Fano factor (a material specific constant), ϵ is the energy necessary to create one electron-hole pair, and E is the gamma-ray energy. Assuming a Fano factor of 0.08 and 2.96 eV for electron-hole production, a broadening (W_D) of 1.32 keV is expected at 1.33 MeV. However the best energy resolution for these detectors tends to be about 1.7 keV. The

interference between the ^{20}F and the ^{38}Cl signals is due to ^{20}F 's gamma ray at 1633.6 keV and ^{38}Cl 's gamma ray at 1642.4 keV. For adequate discrimination, peaks should be at least one FWHM apart, so the HPGe detector will be adequate to resolve the signals if it has not suffered too much degradation.

Using a HPGe detector system confers the benefit of improved resolution while using a NaI(Tl) detector system confers the benefit of increased efficiency. Other detectors whose resolution is not good enough to resolve the peaks of interest are not a worthwhile consideration if they do not have as good of an efficiency as the NaI(Tl) detector system. For example, a lanthanum bromide detector is an unlikely candidate to improve the detection system.

2.3 Methods

2.3.1 Hand Simulating Phantom

When developing an experimental setup, anthropomorphic calibration standards (also referred to as phantoms) are used to minimize the radiation dose given to humans. In an *in vivo* situation, other elements inside the body cause competing reactions, obscuring the desired signals. Thus when

determining the detection limit of a system, it is necessary to use a phantom that will appropriately represent the signal that would be expected when irradiating humans. The phantoms were assembled using dry powder compounds. The compounds used must contain the signal-contributing elements. Any elements in the powders that would not be expected to contribute to the acquired *in vivo* signal during the measurement time must either be negligibly activated or emit radiation that would not be recorded during the measurement time such as prompt gamma rays. The elements and their amounts were chosen based off the hand of the reference man of the International Commission on Radiological Protection (ICRP) [8]. This follows previous work done in our laboratory using hand calibration phantoms [50, 51, 54, 61]. Details of the powders used in the phantoms and their relevant properties are provided in Table 2.1. The phantoms can be held together by a container or some form of binding agent. When designing phantoms to be used in the sodium iodide detection system, it is necessary to use Mowiol as a binding agent as polyethylene bottles produce an aluminum-28 signal in close proximity to the fluorine-20 signal [62]. This is less important when using the HPGe setup as the peaks from aluminum are easily resolvable from the fluorine peaks. The hand phantoms used have been

previously shown to have a very similar signal as compared to *in vivo* situations [54].

	Sodium	Chlorine	Calcium	Fluorine
Mass (g) (\pm .001g)	1.25	1.19	14.9	varying
Relevant Nuclides	^{24}Na	^{38}Cl	^{49}Ca	^{20}F
Half-life	15 hr	37 min	8.8 min	11 s
Gamma Energies (keV)	1368.6, 2754.0	1642.4, 2167.5	3084.4	1633.6
Compound	NaNO_3	NH_4Cl	CaCO_3	NH_4F

Table 2.1: Elemental composition of the hand simulating phantoms, as well as the radionuclides produced following neutron activation and their associated half-lives and daughter gamma-ray energies.

2.3.2 Experimental Detector Setup

Before any measurements could take place, a permit outlining the experimental procedures and radioisotopes to be produced was approved by the McMaster Health Physics department.

Measurements were made on the 4π NaI(Tl) detection system following previous work in the laboratory. The only change in setup was the location of the detectors, which was not directly next to the irradiation cavity as in previous measurements. This was done to avoid relocating the detectors while other experimental studies were going on. Following previous procedures, six 5 s spectra were recorded followed by a 180 s wait period, and

a 300 s count. The 300 s count is performed since the half-life of chlorine-38 is much greater than that of fluorine-20. Thus the second count allows for the precise measurement of ^{38}Cl to be subtracted from other spectra. The calcium-49 count is also determined from this second count so the amount of fluorine can be normalized to the amount of calcium.

The NaI(Tl) set-up has a built-in timing system and spectra can be acquired in singles mode, anti-coincidence mode, or in coincidence mode. In singles mode, each detector records information separately. In coincidence or anti-coincidence mode, the signal from all the detectors for a time period of 1.0–1.8 μs [63] is summed. If two or more detectors are active in that time period, the summed signal is treated as a coincidence event. However, if only one detector signals, then the summed signal is treated as an anti-coincidence event. Thus, it is possible to separate out events in the nine detectors that happen within a certain time interval. True coincidence summing occurs when the coincident detection of photons comes from the same decay event (e.g. a cascade gamma emitter or annihilation photons). Random coincidence summing occurs when the coincident detection of photons comes from different decay events. In any one of the nine sodium iodide detectors, there could be random coincidence summing or true coincidence summing events. In the anti-coincidence spectrum, cascade emitters will be greatly

reduced in comparison to single photon emitters. However, there are limitations to this technique as there will be some reduction in signal from random coincidence summing. As well, this technique is unable to remove coincident events that happen in a single detector. Since ^{38}Cl 's interfering gamma ray at 1642.4 keV is emitted in coincidence with a gamma-ray at 2167.5 keV, anti-coincidence mode helps to remove the interfering signal. Previous work has shown anti-coincidence mode lowers the MDL by a factor of 1.2 [55]. A comparison of anti-coincidence, coincidence, and singles spectra for a measurement is presented in Figure 2.1.

To investigate if the superior energy resolution of HPGe had a significant impact on the ^{18}F MDL, a HPGe detector setup was constructed. The first step was to locate functioning detectors. A number of detectors within the laboratory were analyzed for resolution and efficiency, and the best two chosen. The specifications of the two detectors are displayed in Table 2.2.

Annealing is a common technique used to enhance the resolution of germanium detectors. This has been performed before in our laboratory previously and resulted in improved resolution [64]. The energy resolution of HPGe detectors can often degrade due to neutron damage. To provide the best opportunity for the new setup using HPGe detectors to perform better,

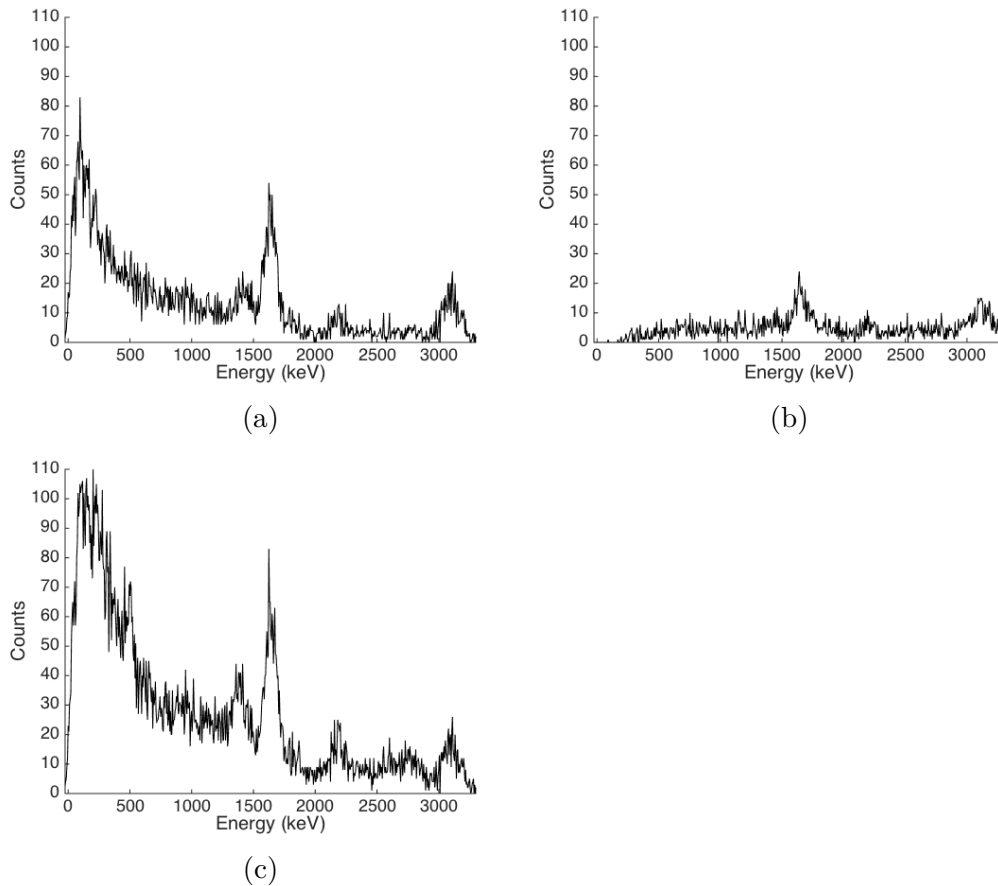


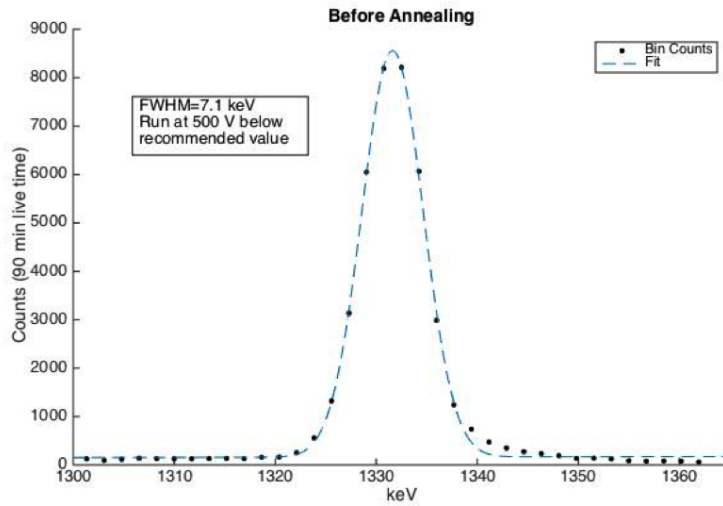
Figure 2.1: 4π NaI(Tl) detection system responses in three different modes to a bone phantom containing 256 mg F that was neutron activated and subsequently measured. The three different modes tested were: anti-coincidence mode (a), coincidence mode (b), and singles mode (c). Chlorine-38's cascade gamma rays result in the peaks seen in (b) at 1642.4 keV and 2167.5 keV. The main peak between 1600 and 1700 keV in (c) is composed of both the fluorine-20 peak at 1633.6 keV and the chlorine-38 peak at 1642.4 keV. The lower energy peak to the left of this peak is a result of the potassium-40 peak at 1460.8 keV and the sodium-24 peak at 1368.6 keV.

one detector was annealed before the experiment. The enhanced performance of the detector is outlined in Figure 2.2. The setup of the two germanium detectors is shown in Figure 2.3.

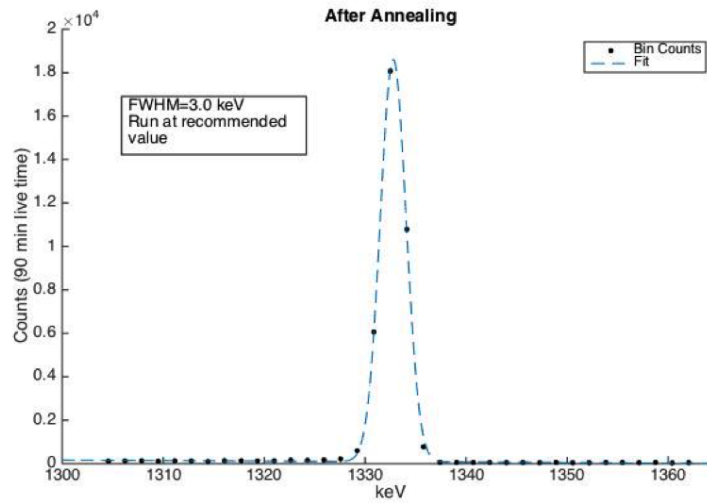
	Detector 1	Detector 2
Semiconductor Type	p-type	p-type
Detector Geometry	coaxial	coaxial
Diameter (mm)	59	58
Length (mm)	47	53
Relative Efficiency (from User's Manual)	30%	30%
Bias Voltage	+4000 V	+5000 V
Manufacturer	Canberra	Canberra
Cryostat	Dipstick	Integral

Table 2.2: Basic properties of the two HPGe detectors used in the experimental work.

Timing was set up for the germanium detectors using Maestro software, and a 92x spectrometer was used to process the signals. Within the Maestro software, there is an option to automate data collection using a job file. Data were collected in 5 s intervals for a total of 150 s. The detectors were both calibrated using a cobalt-60 source which emits gamma rays at 1173.2 keV and 1332.5 keV. Calibration of the NaI(Tl) system takes much longer as each detector's gain must be set so that the calibration peaks are aligned. For the HPGe system, calibration is done simply to convert the peak channel numbers into energy bins.



(a)



(b)

Figure 2.2: Energy resolution of HPGe Detector 1 to cobalt-60's 1332.5 peak before (a) and after (b) annealing. The FWHM was reduced by 4.0 keV, bringing it to a value of 3.0 keV, which is still sub-optimal but adequate to resolve the fluorine-20 and chlorine-38 peaks.

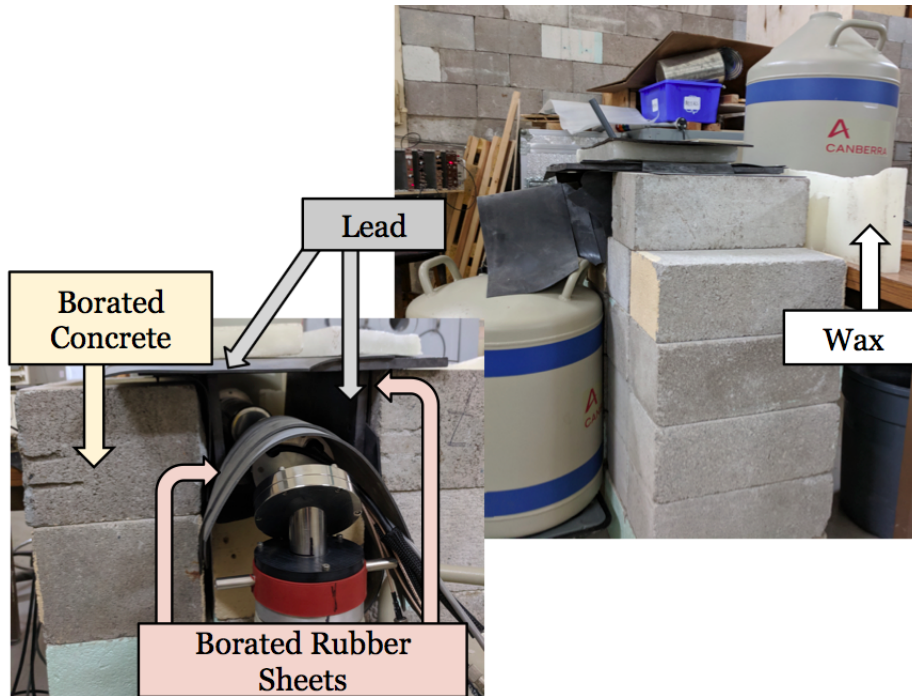


Figure 2.3: Experimental setup of HPGe Detector 1 (left) and HPGe Detector 2 (right) including borated concrete, lead, borated rubber sheets, and wax for shielding of both gamma rays and neutrons.

2.3.3 Irradiation Protocol

The irradiation protocol was a $500 \mu\text{A}$ current of 2.15 MeV protons with an 8 s irradiation. The tandem accelerator had been previously run at higher current, but has since suffered performance issues. This protocol was chosen to maximize signal while still keeping the effective dose below a reasonable amount of $35 \mu\text{Sv}$ [54,55,65]. This dose is mainly due to neutrons, and gammas produced from activation of the box materials.

There was a 15 s transfer time between irradiation and measurement. Previous experiments had a 9 s transfer time, but to avoid relocating the detectors while other work was going on, it was decided to keep the timing consistent at 15 s. As long as the timing remains consistent between measurement techniques, a comparison can still be made.

2.3.4 Calculating a Minimum Detection Limit

Minimum Detection Limit - Signal

When measuring any analyte, it is important to know how sensitive the detection system is. There is always some uncertainty associated with any measurement, even if it is taken under conditions where there is no nuclide present. Knowing what the smallest amount of analyte is that can be reliably detected provides a metric of the detection system's sensitivity. There are many metrics used and reported in a variety of fields including: instrument detection limit (IDL), practical quantification limit (PQL), limit of quantification (LOQ), limit of detection (LOD), limit of decision (LOD), limit of blank (LOB). Going forward, the metric used in this thesis will be the minimum detection limit (MDL). The MDL sets a value on how much signal is necessary to differentiate the signal from background events. The

calculation method for this number varies from laboratory to laboratory depending on what is being measured and the confidence interval required. Determination of the MDL should be performed at different times and by different research staff to ensure its reliability. It can be calculated from blank samples or spiked samples near the MDL (typically at 2–10x the hypothesized MDL). The United States Environmental Protection Agency defines the method detection limit as the minimum measured concentration that can be reported with 99% confidence to be distinguishable from blank results [66].

$$\text{Method Detection Limit} = t_{n-1, 1-\alpha=0.99} S_s, \quad (2.5)$$

where $t_{n-1, 1-\alpha=0.99}$ is the Student's t -value appropriate for a single-tailed 99th percentile t statistic and a standard deviation estimate with $n - 1$ degrees of freedom and S_s is the sample standard deviation of the replicate spiked sample analyses.

Radiation decays are modelled by a Poisson parent distribution where the variance is equal to the mean. Thus, both the sample mean and the sample variance (multiplied by $N/(N - 1)$) are unbiased estimators of the variance. The sample variance can be used for multiple measurements. In

an *in vivo* situation, where increasing the repetitive number of measurements might not be feasible due to time or radiation dose limitations, it often makes sense to do a single measurement and report that as the variance.

Following past work determining the MDL from gamma spectrometers [67], the MDL is the addition of the term $k\sigma_0$, defined as the critical level L_C , which determines how often a blank sample will be correctly identified as zero, and the term $k\sigma_D$ which determines how often an amount right at the detection limit will be correctly identified as a signal. The k value corresponds to a certain z-score, σ_D is the standard deviation right at the detection limit, and σ_0 is the standard deviation of the blank sample. The MDL may therefore be calculated via

$$\text{MDL} = k\sigma_0 + k\sigma_D . \tag{2.6}$$

The variance of a sample at the detection limit is given by:

$$\sigma_D^2 = C_G + C_B \tag{2.7}$$

$$= (\text{MDL} + C_B) + C_B , \tag{2.8}$$

where C_G is the gross counts, C_B is the background counts, and C_N is the net counts.

The variance of a zero concentration sample is given by

$$\sigma_0^2 = C_G + C_B \quad (2.9)$$

$$= C_N + 2C_B \quad (2.10)$$

$$= 2C_B . \quad (2.11)$$

Putting these equations together, setting the k value to be the same in both equations, and re-arranging:

$$\text{MDL} = k^2 + 2k\sigma_0 . \quad (2.12)$$

In general, the k^2 term is negligible and the expression may be simplified to

$$\text{MDL} = 2k\sigma_0 . \quad (2.13)$$

For $k = 1$, which is the value typically used in our laboratory, Equation 2.13 yields a degree of confidence of 84.13% based off the cumulative standard

normal distribution. If the σ_0 refers to the number of counts that is distinguishable from background, then the MDL calculation simplifies to

$$\text{MDL} = 2\sqrt{2C_B} . \quad (2.14)$$

Fluorine to Calcium Ratio

The goal of gamma-ray spectroscopy is to identify and quantify gamma-ray emitting radionuclides by determining the number of detected counts corresponding to a gamma ray at a specific energy. In an ideal radiation detector, there would be a delta spike at the energy of interest. However, due to the physical restrictions of the detector, the detected signal may be approximated as a Gaussian peak centred at the energy of interest. The width of this peak is determined by the detector's properties. Thus, a range of energies must be inspected when determining the number of counts from a specific gamma ray. The number of counts within this range of energies is affected not only by gamma rays of the energy of interest, but also by other competing processes such as Compton scattering from higher energy gamma rays. All other competing processes are collectively referred to as background events. Thus when performing gamma spectroscopy, a method for determining the size of the inspected energy range and a method for

determining true events from background events are necessary. A common approach is to take the number of channels (n) where data are collected to be determined by the full width at one-tenth maximum peak height (FWTM), while assuming that the background counts can be approximated by a linear function (which is reasonable over a narrow energy interval) [59]. The linear function of the background and the FWTM are determined by fitting the peak as a Gaussian function with a linear background using a fitting algorithm. The area of the fitted Gaussian peak may be used to determine the number of counts. Alternatively, the total counts in each channel were counted, and the estimate for the linear background subtracted as there is then no fitting error in the peak counts calculation. The error in a peak is given by

$$\sigma^2 = C_G + C_B \quad (2.15)$$

$$= C_N + 2C_B . \quad (2.16)$$

Since the resolution of the sodium iodide detectors is significantly poorer than that of the HPGe detectors, it is necessary to subtract the fraction of the peak containing the fluorine-20 signal which corresponds to chlorine-38. Determining the fraction of chlorine-38 in the signal was done by acquiring a

300 s spectrum 180 s following the last measurement when the fluorine signal was negligible, and any counts in the 1.64 MeV peak will be from chlorine-38. The amount of chlorine-38 in the initial measurement may be calculated by either using the known intensity ratio between the two chlorine peaks as was done in Ref. [54], or by using the nuclear decay kinetics.

If m is determined by the equation

$$m = n - \frac{qp}{r}, \quad (2.17)$$

where n , q , p , and r are variables, and the covariance is assumed to be zero, the error σ_m will be given by

$$\sigma_m^2 = \left| \frac{\partial m}{\partial n} \right|^2 \sigma_n^2 + \left| \frac{\partial m}{\partial p} \right|^2 \sigma_p^2 + \left| \frac{\partial m}{\partial q} \right|^2 \sigma_q^2 + \left| \frac{\partial m}{\partial r} \right|^2 \sigma_r^2 \quad (2.18)$$

$$\sigma_m^2 = \sigma_n^2 + \frac{q^2}{r^2} \sigma_p^2 + \frac{p^2}{r^2} \sigma_q^2 + \frac{q^2 p^2}{r^4} \sigma_r^2. \quad (2.19)$$

Equation 2.17 and 2.19 can be used to calculate the number of fluorine-20 counts during the measurement period using the peak subtraction method where m is the number of fluorine-20 counts in the counting period, n is the

total counts from both the fluorine-20 1633.6 keV peak and the chlorine-38 1642.4 keV peak during the counting period, p is the number of counts in chlorine-38's 2167.5 keV peak during the counting period, q is the number of counts in chlorine-38's 1642.4 keV peak during the 300s period, and r is the number of counts in chlorine-38's 2167.5 keV peak during the 300 s period. To determine the number of counts using the nuclear decay kinetics method, the equation

$$m = n - q * C1 , \quad (2.20)$$

can be used where $C1$ is a constant equal to

$$C1 = \frac{1}{(1 - e^{-\lambda(300s)})(e^{-\lambda(210s)})} - \frac{1}{(1 - e^{-\lambda(300s)})(e^{-\lambda(180s)})} , \quad (2.21)$$

and λ is the decay constant of chlorine-38 ($\lambda = .00031s^{-1}$). Assuming that the time and the half-life uncertainty contribute a negligible amount to the total uncertainty, the error of m for this calculation will be given by

$$\sigma_m^2 = \left| \frac{\partial_m}{\partial_n} \right|^2 \sigma_n^2 + \left| \frac{\partial_m}{\partial_q} \right|^2 \sigma_q^2 \quad (2.22)$$

$$\sigma_m^2 = \sigma_n^2 + C1^2 \sigma_q^2. \quad (2.23)$$

Using both methods to calculate the fluorine-20 counts and associated errors yielded very similar results. The exponential decay method had slightly smaller errors and was used to determine the number of fluorine-20 counts in the measurement period as well as associated error.

Since in this experiment, the fluorine peak is normalized to the calcium peak, the σ_0 in the equation for the MDL will not be simply the fluorine peak uncertainty, but the F/Ca ratio uncertainty of the zero-concentration phantom. If a function is given by

$$f = a/b, \quad (2.24)$$

the error is given by

$$\sigma_f^2 = \left| \frac{\partial f}{\partial a} \right|^2 \sigma_a^2 + \left| \frac{\partial f}{\partial b} \right|^2 \sigma_b^2 + 2 \frac{\partial f}{\partial a} \frac{\partial f}{\partial b} \sigma_{ab} \quad (2.25)$$

$$\sigma_f^2 = \frac{\sigma_a^2}{b^2} + \frac{a^2 \sigma_b^2}{b^4} - 2 \frac{a \sigma_{ab}}{b^3} . \quad (2.26)$$

This equation is used for the calculation of the F/Ca ratio error with $f = \text{F/Ca ratio}$, $a = \text{F counts}$, and $b = \text{Ca counts}$. Assuming the covariance between the ^{49}Ca and ^{19}F peak is zero, the error for the F/Ca ratio is given by

$$\sigma_{\text{F/Ca}}^2 = \frac{\sigma_{\text{F}}^2}{\text{Counts}_{\text{Ca}}^2} + \frac{\text{Counts}_{\text{F}}^2 \sigma_{\text{Ca}}^2}{\text{Counts}_{\text{Ca}}^4} . \quad (2.27)$$

This was the calculation used to determine the error of the calibration line points. For the zero-concentration phantom, where $\text{Counts}_{\text{F}} = 0$,

$$\sigma_{\text{F/Ca}}^2 = \frac{\sigma_0^2}{\text{Counts}_{\text{Ca}}^2} . \quad (2.28)$$

Conversion of count data to concentrations

Usually, it is not the minimum number of counts that is detectable above background that is of interest, but the concentration of the analyte of interest that corresponds to the number of counts. It is for this reason that phantoms with differing concentrations of fluorine were measured. The F/Ca ratios are plotted against the known concentrations of the phantoms, and a weighted least squares regression was performed to calculate the calibration line. The points have differing variations (heteroscedastic), and are weighted inversely to their variance, so more confidence is placed on points with less uncertainty. To do this, it is assumed that the errors are normally distributed and that the differences between the regression line and the experimental data are only caused by errors in the F/Ca ratio (the y-values), as opposed to the phantom concentrations (the x-values). The equation for a regression line is

$$y = a + bx , \tag{2.29}$$

where a is the estimated y-intercept, b is the estimated slope, and for our experiment, y is the measured F/Ca peak ratios, and x is the known mg F/g Ca phantom concentrations. Assuming that each individual measure of y_i is

taken from a Gaussian parent distribution with mean y_0 and standard deviation σ_i , the probability distribution P_i will have the form

$$P_i = \frac{1}{\sigma_i \sqrt{2\pi}} e^{-\frac{1}{2} \left[\frac{y_i - y(x_i)}{\sigma_i} \right]^2}, \quad (2.30)$$

and the probability of a set of measurements will be each individual probability multiplied. To maximize the probability of getting a certain set of experimental values from the hypothesized parent distribution calibration line, the χ^2 term is minimized:

$$\chi^2 = \sum \left[\frac{y_i - y(x_i)}{\sigma_i} \right]^2 \quad (2.31)$$

$$= \sum \left[\frac{y_i - a - bx_i}{\sigma_i} \right]^2. \quad (2.32)$$

Following the approach of Bevington and Robinson [68], the partial derivatives with respect to a and b are set to zero, yielding two equations for the two unknowns of a and b , which can be determined analytically as

$$a = \frac{1}{\Delta} \left(\sum \frac{x_i^2}{\sigma_i^2} \sum \frac{y_i}{\sigma_i^2} - \sum \frac{x_i}{\sigma_i^2} \sum \frac{x_i y_i}{\sigma_i^2} \right) \quad (2.33)$$

$$b = \frac{1}{\Delta} \left(\sum \frac{1}{\sigma_i^2} \sum \frac{x_i y_i}{\sigma_i^2} - \sum \frac{x_i}{\sigma_i^2} \sum \frac{y_i}{\sigma_i^2} \right) \quad (2.34)$$

$$\Delta = \sum \frac{1}{\sigma_i^2} \sum \frac{x_i^2}{\sigma_i^2} - \left(\sum \frac{x_i}{\sigma_i^2} \right)^2. \quad (2.35)$$

The above equations calculate the calibration line coefficients which are inversely weighted by the variance. However, the equations for the slope and y-intercept are estimates and come with associated error that must be accounted for when going from the measured F/Ca peak ratios ratio to the phantom concentrations (mg F/g Ca).

It was previously assumed that all of the error was coming from the y-values. To calculate the total error, ignoring systematic errors that would introduce correlations between uncertainties, the variance of a parameter a , is given by [68]

$$\sigma_a^2 = \sum \left[\sigma_i^2 \left(\frac{\partial a}{\partial y_i} \right)^2 \right]. \quad (2.36)$$

Similarly, the covariance between a and b is given by [68]

$$\sigma_{ab} = \sum \left[\sigma_i^2 \frac{\partial a}{\partial y_i} \frac{\partial b}{\partial y_i} \right]. \quad (2.37)$$

Calculating the partial derivatives and putting them in the equations, the variances of a and b , and the covariance between a and b are calculated as:

$$\sigma_a^2 = \frac{1}{\Delta} \sum \frac{x_i^2}{\sigma_i^2} \quad (2.38)$$

$$\sigma_b^2 = \frac{1}{\Delta} \sum \frac{1}{\sigma_i^2} \quad (2.39)$$

$$\sigma_{ab} = -\frac{1}{\Delta} \sum \frac{x_i}{\sigma_i^2}. \quad (2.40)$$

The y-intercept and slope are used to back-calculate the initial concentration (x) in mg F/g Ca by

$$x = \frac{y - a}{b}. \quad (2.41)$$

The uncertainty in x will be given by

$$\begin{aligned}
 \sigma_x^2 &= \left| \frac{\partial x}{\partial y} \right|^2 \sigma_y^2 + \left| \frac{\partial x}{\partial a} \right|^2 \sigma_a^2 + \left| \frac{\partial x}{\partial b} \right|^2 \sigma_b^2 + 2 \frac{\partial x}{\partial a} \frac{\partial x}{\partial b} \sigma_{ab} \\
 \sigma_x^2 &= \frac{\sigma_y^2}{b^2} + \frac{\sigma_a^2}{b^2} + \frac{(y^2 - 2ya + a^2)\sigma_b^2}{b^4} + 2 \frac{(y - a)\sigma_{ab}}{b^3}. \quad (2.42)
 \end{aligned}$$

In the case of the zero-concentration phantom, this reduces to

$$\sigma_0^2 = \frac{\sigma_y^2}{b^2} + \frac{\sigma_a^2}{b^2} + \frac{a^2\sigma_b^2}{b^4} - 2 \frac{a\sigma_{ab}}{b^3}, \quad (2.43)$$

which follows previous calculations for the MDL in our laboratory [69].

Multiple MDL Estimates

It is possible to get multiple calculations of the MDL. This could be from either multiple gamma rays of the nuclide of interest, having multiple detectors collecting data, or from breaking up the measurement into separate time intervals. The more estimates there are of a number, the smaller the variance should be, and the smaller the MDL. For example, if there are two estimates of a concentration: $X_1 \pm \sigma_{X_1}$ and $X_2 \pm \sigma_{X_2}$, and the average X_{ave} is equal to

$$X_{\text{ave}} = \frac{X_1 + X_2}{2}, \quad (2.44)$$

the variance is given by

$$\sigma_{X_{\text{ave}}}^2 = \left(\frac{\partial X_{\text{ave}}}{\partial X_1} \right)^2 \sigma_{X_1}^2 + \left(\frac{\partial X_{\text{ave}}}{\partial X_2} \right)^2 \sigma_{X_2}^2 \quad (2.45)$$

$$= \left(\frac{1}{2} \right)^2 \sigma_{X_1}^2 + \left(\frac{1}{2} \right)^2 \sigma_{X_2}^2. \quad (2.46)$$

In general, the equation for the variance of an average of i measurements is given by

$$\sigma^2 = \frac{\sigma_i^2}{i^2}. \quad (2.47)$$

Thus, the total MDL for a set of i measurements will be equal to

$$\text{MDL}_{\text{total}} = \sqrt{\frac{\sum_i \text{MDL}_i^2}{i}}. \quad (2.48)$$

Instead of a direct calculation of the MDL, a weighted calculation may be performed, where concentration estimates with a smaller variance have a higher weight. The formula for this would have the form

$$X_{\text{ave}} = \frac{\sum(X_i/\sigma_i^2)}{\sum(1/\sigma_i^2)}. \quad (2.49)$$

If there are two measurements, the variance of the weighted average will be given by

$$\sigma_{X_{\text{average}}}^2 = \left(\frac{\partial X_{\text{average}}}{\partial X_1}\right)^2 \sigma_{X_1}^2 + \left(\frac{\partial X_{\text{average}}}{\partial X_2}\right)^2 \sigma_{X_2}^2 \quad (2.50)$$

$$= \left(\frac{1/\sigma_{X_1}^2}{1/\sigma_{X_1}^2 + 1/\sigma_{X_2}^2}\right) \sigma_{X_1}^2 + \left(\frac{1/\sigma_{X_2}^2}{1/\sigma_{X_1}^2 + 1/\sigma_{X_2}^2}\right) \sigma_{X_2}^2 \quad (2.51)$$

$$= \frac{1/\sigma_{X_1}^2 + 1/\sigma_{X_2}^2}{1/\sigma_{X_1}^4 + 1/\sigma_{X_2}^4} \quad (2.52)$$

$$= \frac{1}{1/\sigma_{X_1}^2 + 1/\sigma_{X_2}^2}. \quad (2.53)$$

So in the weighted average calculation, the general formula for i measurements will be given by :

$$\sigma^2 = \frac{1}{\sum(1/\sigma_i^2)}. \quad (2.54)$$

Thus, the total MDL for a set of i measurements for an inverse-variance weighted average will be equal to

$$\text{MDL}_{\text{total}} = \sqrt{\frac{1}{\sum 1/\text{MDL}_i^2}}. \quad (2.55)$$

These calculations follow previous work done in our laboratory [54, 69]. In the case of the high-purity germanium detector system, where the data from each detector are analyzed separately, an MDL is calculated for each detector. These MDLs can be combined together to form the MDL of the whole detection system.

2.4 Results

The detector response function of the two high-purity germanium detectors to the 1332.5 keV peak of cobalt-60 is presented in Figure 2.4. Commonly reported performance metrics were calculated from the collected spectra and are displayed in Table 2.3.

Experimental spectra of the first 30 s of measurement following irradiation and transfer time to the HPGe Detector 1, HPGe Detector 2, and

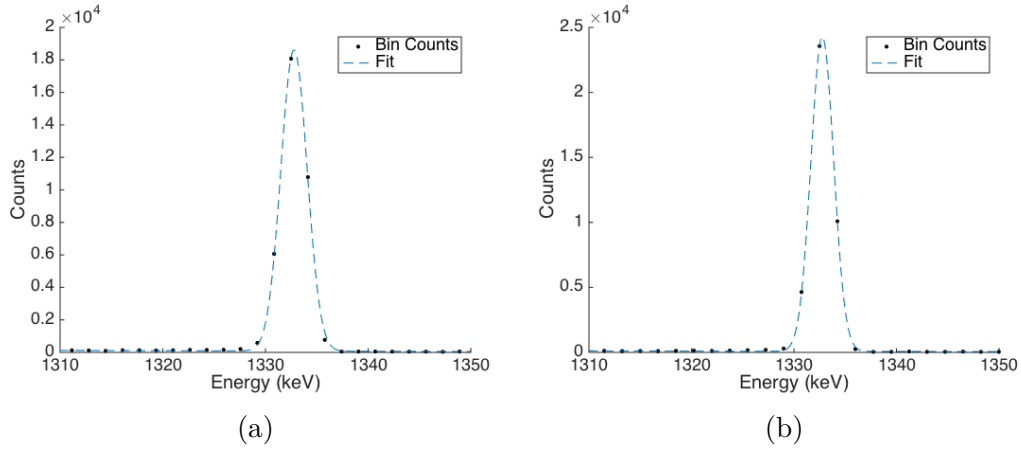


Figure 2.4: Detector response function of HPGe Detector 1 (a) and HPGe Detector 2 (b) to the 1332.5 keV peak of Co-60.

	FWHM	Peak-to-Compton Ratio	Absolute Efficiency	Relative Efficiency
Detector 1	2.6	35	1.9E-04	0.16
Detector 2	3.0	29	1.8E-04	0.15

Table 2.3: HPGe detector performance metrics including: FWHM, Peak-to-Compton ratio, absolute detection efficiency with a source to detector difference of 25 cm, and relative efficiency compared to a 3" by 3" NaI(Tl) detector.

the NaI(Tl) anti-coincidence detection system are shown in Figure 2.5,

Figure 2.6, and Figure 2.7 respectively. These spectra illustrate the

differences in resolution and detected counts between the two measurement systems. Measurement spectra from a 256 mg F (18 mg F/g Ca) phantom as well as a background where no phantom was placed in the detection system were both collected. The background spectra taken with no phantom show the contribution to the measured phantom spectra which is attributable to counts coming from the experimental protocol and not the hand phantom.

The Compton continuum in the spectra from no phantom is at a lower count rate than the Compton continuum in the phantom spectra. This is to be expected as gamma rays from the activated elements in the phantoms will contribute to the Compton continuum. There is a peak at 1460.8 keV in all of the spectra that can be attributed to potassium-40's peak at 1460.8 keV.

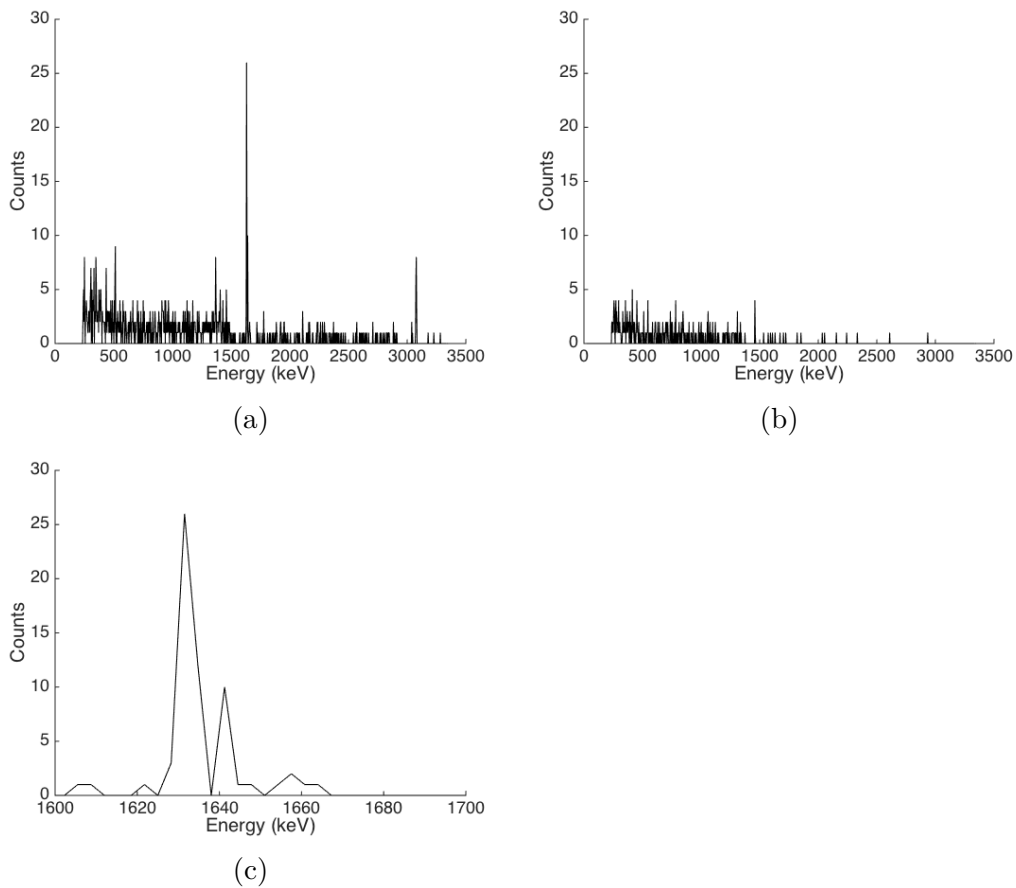


Figure 2.5: Measurement spectra collected on HPGe Detector 1 for 30 s following neutron irradiation and a 15 s transfer time of: a 256 mg F phantom (a), no phantom (b), and the same 256 mg F phantom displayed in a smaller energy region corresponding to the fluorine-20 peak (c).

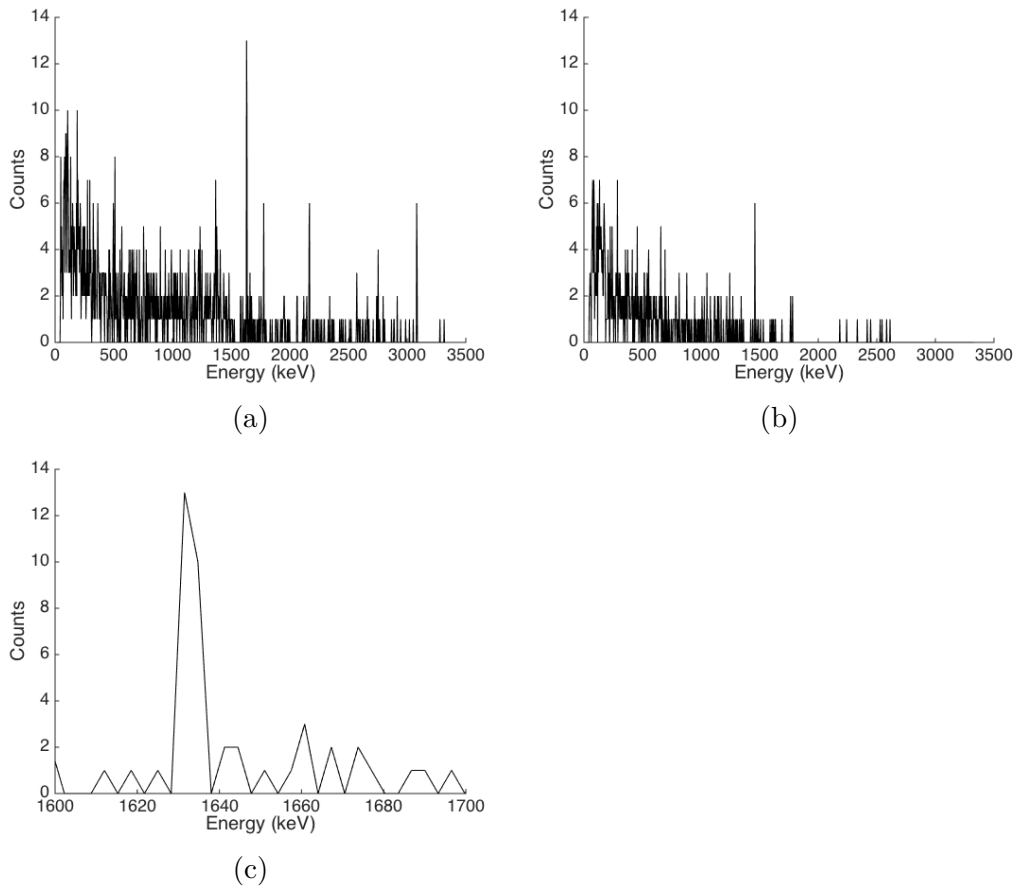


Figure 2.6: Measurement spectra collected on HPGe Detector 2 for 30 s following neutron irradiation and a 15 s transfer time of: a 256 mg F phantom (a), no phantom (b), and the same 256 mg F phantom displayed in a smaller energy region corresponding to the fluorine-20 peak (c).

Fluorine to calcium ratios and associated errors were calculated as described in Equations 2.16 and 2.27 for each F-phantom irradiation and data collection. Equations 2.23 and 2.20 were also used for the NaI(Tl) system to determine the fluorine-20 counts and errors. These were plotted to construct a calibration for each detector. The calibration lines are presented in Figures 2.8, 2.9, 2.10. The slope and y-intercept along with associated

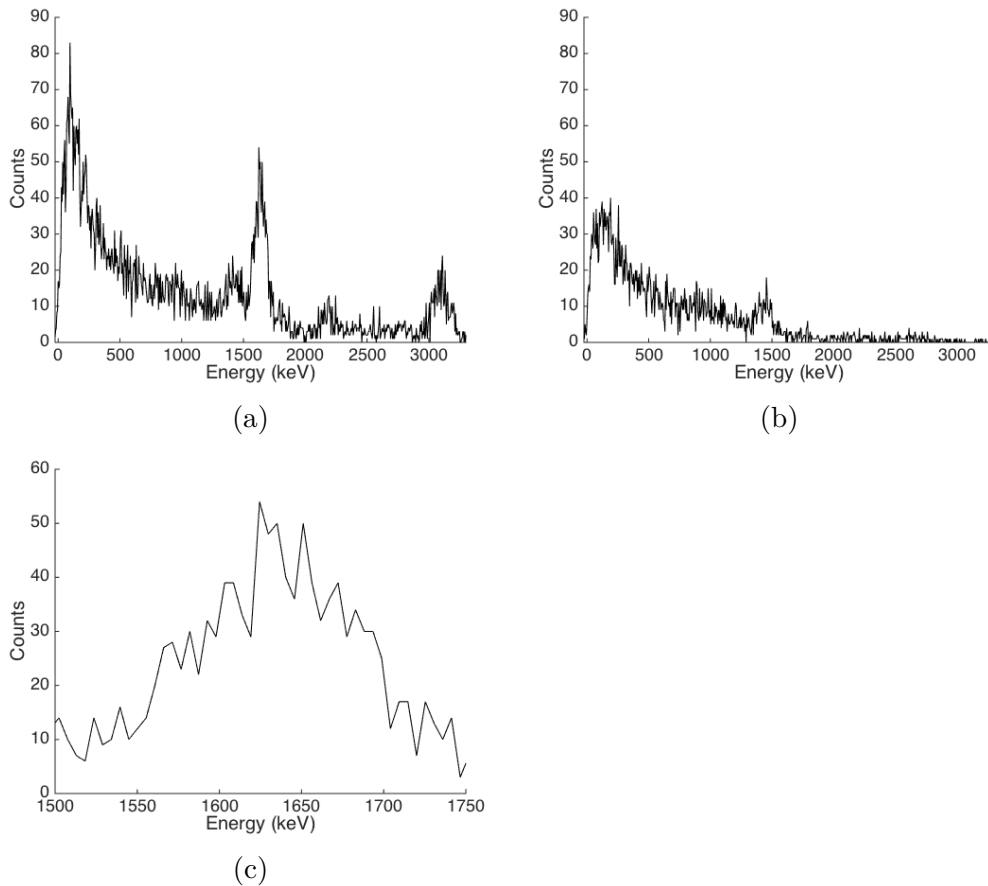


Figure 2.7: Measurement spectra collected on the NaI(Tl) system for 30 s following neutron irradiation and a 15 s transfer time of: a 256 mg F phantom (a), no phantom (b), and the same 256 mg F phantom displayed in a smaller energy region corresponding to the fluorine-20 peak (c).

errors were calculated using Equations 2.33, 2.34, 2.35, 2.38, and 2.39. The χ^2 was calculated from Equation 2.32. The F/Ca ratio uncertainty in the zero-concentration phantom was determined as per equations 2.11 and 2.28, and averaged over all measurements. Following equations 2.43 and 2.55, the combined HPGe detection system MDL was found to be 4.6 mg F/g Ca. The sodium iodide detection system MDL was calculated to be 0.95 mg F/g Ca.

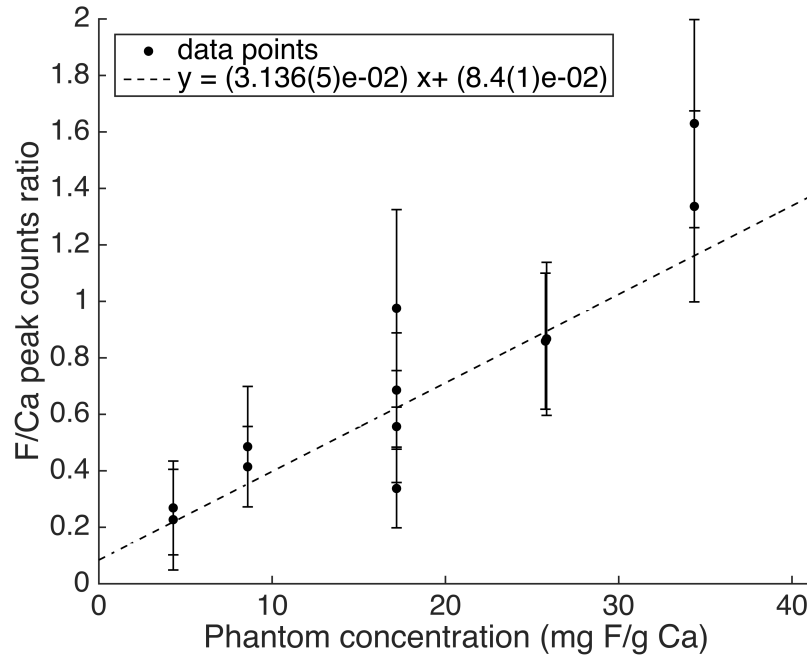


Figure 2.8: Calibration line determining the relationship between the experimental F/Ca peak ratios and associated errors to the known concentrations of the phantom in mg F/g Ca for HPGe Detector 1 ($\chi^2 = 8.0$).

2.5 Discussion

Even though the HPGe detector specifications are similar as shown in Table 2.2, there were sometimes significant differences in the number of counts recorded by each HPGe detector. This is made clear while comparing the spectra in Figures 2.5 and 2.6. The differences in response are most likely due to variation in the sample placement. Comparing several spectra from the two detectors of the same measurement, no one detector consistently had more counts than the other.

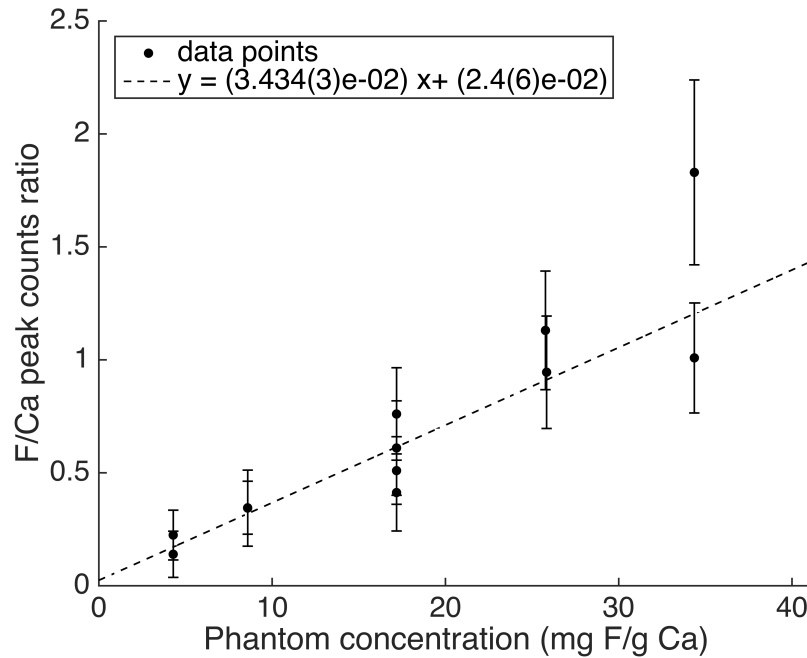


Figure 2.9: Calibration line determining the relationship between the experimental F/Ca peak ratios and associated errors to the known concentrations of the phantom in mg F/g Ca for HPGe Detector 2 ($\chi^2 = 6.5$).

Previous work using the NaI(Tl) system found a detection limit of 0.17 mg F/g using an inverse variance weighted method (IVWM) for 5 s timing intervals, and a detection limit of 0.24 mg F/g Ca using a 30 s timing segment [55]. A small study of an HPGe detector was also performed and the detection limit calculated as 0.71 mg F/g Ca [55]. An MDL comparison of previously reported values to the experimental values is shown in Table 2.4. Thus, the detection limit of the HPGe system was closer to the detection limit of the NaI(Tl) system in the previous work than it was in the current experiments. This was not expected as the use of multiple detectors in the

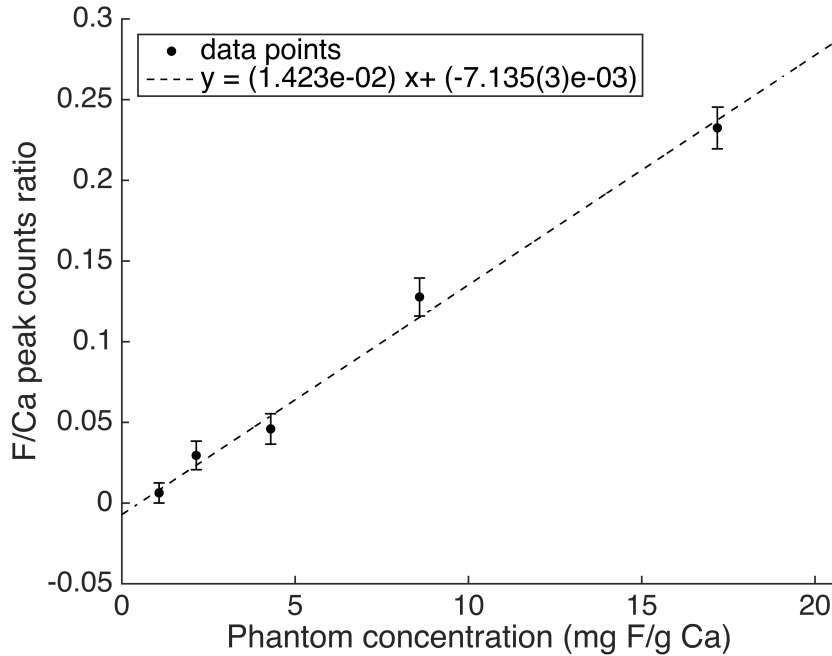


Figure 2.10: Calibration line determining the relationship between the experimental F/Ca peak ratios and associated errors to the known concentrations of the phantom in mg F/g Ca for the NaI(Tl) detection system ($\chi^2 = 2.6$).

HPGe setup was hypothesized to bring the HPGe setup's MDL closer to the NaI(Tl) setup's MDL. This unexpected result may be due to differences in the placement of the phantoms resulting in a smaller solid angle being measured. The previous work using HPGe measured the phantom directly at the detector face. This is not a realistic model of an *in vivo* measurement as a hand is wider and flatter than a phantom and would be greater than the size of the detector face. Differences in the calculation method of the MDL or differing detector efficiencies would also have an effect. Both the NaI(Tl) system MDL and HPGe system MDL increased in the current experimental

work. This was expected as the the transfer time between irradiation and measurement was longer. Since the transfer time was increased from an average of 9 s to a pre-determined value of 15 s, the activity of fluorine in the previous measurements would have been 1.5x greater than the activity of fluorine in the current experimental work. This explains some of the difference in the MDLs, however it cannot be the only factor affecting the increase in MDL. Other factors that may have contributed to the difference in MDLs could be differences in the MDL calculation method, changes in the neutron beam, poor alignment of the NaI(Tl) channels, or differences in phantom placement inside the irradiation cavity. By increasing the number of data points collected for the calibration lines, it may also be possible to minimize the contribution to the MDL from uncertainty in the calibration line coefficients.

	Experimental MDL	Past MDL
HPGe setup	4.6 mg F/g Ca	0.71 mg F/g Ca
NaI(Tl) setup	0.95 mg F/g Ca	0.24 mg F/g Ca

Table 2.4: Comparison between previously determined MDL values and current experimental MDL values using 30 s measurement times for the NaI(Tl) system and 150 s measurement times for the HPGe system.

There are several parameters that could be optimized to further reduce the MDL of the HPGe system. One of these parameters would be the timing segments. The spectra for the HPGe system were collected in 5

intervals, however analysis was only performed on the spectra obtained after 150 s of measurement. Further work determining the optimal measurement timing parameters and an inverse-variance weighted approach may be able to reduce the detection limit. The use of more HPGe detectors could also further reduce the MDL, until a 4π geometry is attained. The greatest reduction of the MDL would come from the use of higher efficiency detectors, as they would increase the number of fluorine-20 counts detected. However, higher efficiency detectors are more expensive, and there is an upper limit on the size of the germanium crystal.

If the detection limit of the HPGe system could be brought down to a level comparable to the NaI(Tl) system, there would be several considerations to be made when deciding which detection system would be preferable. First, it would be advantageous to prove that the HPGe signal corresponding to the phantoms is in good agreement with a human measurement. This has been done previously on the NaI(Tl) system [54], but has not been done yet using the HPGe system. Provided that the HPGe phantom response was representative of a human signal, further considerations would have to be made. One advantage the HPGe system has is that it doesn't require tedious gain-matching through alignment of channels before every measurement. However, the HPGe detection system

does see performance degradation over time and would have to be properly shielded from neutrons to ensure no resolution degradation.

Further reductions in the detection limit could be possible through the use of other data analysis techniques. One such technique could be spectral decomposition, a technique that uses all of the counts in the spectrum, instead of just the photopeak. A library of detector response functions corresponding to the relevant elements is made and the spectra are matched to this library by varying the intensities of the response functions. This has been previously shown to lower the detection limit when analyzing aluminum by a factor of 1.7 [70]. This technique would most likely have greater benefit for the NaI(Tl) system, as opposed to the HPGe, as there are a much higher number of counts outside the photopeak. However, gain shifts between the detector units and neutron fluence rate variations have been found to be a problem for this method. Other work attempting this method found no significant increase in performance while using the spectral decomposition method [71].

When performing *in vivo* measurements, there are several other considerations. An alternative to using the increased performance of the detection system to lower the detection limit would be instead to use that

increased performance to reduce the dose given to participants. This might improve the chances of ethics approvals or of recruitment success when finding volunteers. When performing phantom measurements, the change in the flux of the neutrons is accounted for by way of normalization to calcium. For a phantom study, this is appropriate as the amount of calcium stays constant. However in a human measurement, the amount of calcium is variable. Thus, the calcium activation measurement is affected by two variables - the neutron count, as well as the amount of calcium in the hand. A second measurement of neutron flux is necessary, so that the calcium measurement determines the ratio of fluorine to calcium, while the second measurement corrects for changes in the neutron flux. Current work in the laboratory is underway to find an appropriate measure of neutron count, as current measures including a neutron detector inside the irradiation cavity, the integrated current of the beam, and neutron foils give inconsistent results. This is something that should be explored further before future human measurement studies.

An important distinction to keep in mind when comparing detection limits of different measurement techniques is that a detection limit of 1 mg F/g Ca in the NAA system does not mean that 1 mg of Fluorine is actually detectable. It means that based on an average amount of 14.9 g of calcium in the hand, that is the ratio of F/Ca that would be detectable. When

comparing with other techniques, it might be preferable to provide a detection limit in terms of the sensitivity of detecting the total fluorine amount in the hand. So, instead of a 1 mg F/g Ca MDL, a 15 mg F MDL could be quoted. Provided that the performance of the experiment could be brought down to the previous MDL of 0.17 mg F/g Ca, this would correspond to a 2.6 mg sensitivity.

Chapter 3

Nuclear Magnetic Resonance

Experiments

3.1 NMR Background

3.1.1 Origin of the Signal

Spin is a quantum mechanical physical property carried by particles and atomic nuclei. The spin value of an atomic nucleus may be determined from the number of neutrons and protons inside that nucleus using the nuclear shell model [72]. Spin is a form of angular momentum which causes the

nucleus to have a magnetic moment; thus, a nucleus with spin can be imagined as a rotating magnetic dipole. The spin angular momentum (I) and the magnetic moment (μ) are proportional to each other [73] via

$$\mu = \gamma I . \tag{3.1}$$

The proportionality constant γ is unique for each individual nuclide and is called the gyromagnetic or magnetogyric ratio. If the ratio of magnetic moment to spin was not unique, NMR would be limited as an analytical technique as different nuclides in the same magnetic field would no longer be differentiable.

Applied magnetic fields impose torques on objects with magnetic moments, and so also impose torque on objects with spin. The torque τ on a magnet with dipole moment μ from a magnetic field B is given by:

$$\tau = \mu \times B . \tag{3.2}$$

An applied torque causes a rotating magnetic moment to precess in the same way a top precesses due to the force of gravity. Thus, when an external

magnetic field B_0 is applied, the nucleus precesses. The rate of precession ω is determined by the strength of the applied magnetic field and the gyromagnetic ratio of the nucleus [73] via

$$\omega = \gamma B_0 . \tag{3.3}$$

With no magnetic field applied, all spins in a collection of nuclei are oriented randomly and there is no net magnetization. When an external magnetic field is applied, there is a slight bias for the spins to align in the direction of the magnetic field [74] (typically referred to as the longitudinal direction). Applying a radiofrequency wave at the precessional frequency, known as the Larmor frequency, perpendicular to the main external field B_0 , imparts a time-varying torque on the magnetic moments due to the oscillating magnetic field B_1 of the radio wave. The radiofrequency field rotates the spin distribution into the transverse plane. The area of the radiofrequency pulse determines the amount of torque applied and the degree of rotation of the spin system (also known as the flip or the tip angle). The magnetization measured in one dimension in the transverse plane oscillates from negative to positive values due to the rotating B_1 field. A changing magnetic moment causes a changing electric field, and so the transverse magnetization is

measurable with a radiofrequency detector. The signal measured is called the free induction decay (FID). The FID is Fourier transformed when performing analysis to examine the frequencies that compose the signal.

3.1.2 Parameters Affecting the Signal

When a B_1 magnetic field is applied, the number of spins realigning in the direction of the B_0 field does not immediately change. Instead, it is a gradual process which depends on the nuclide, the magnetic field, and the molecular binding structure [75]. This is called spin-lattice relaxation, where the amount of time it takes for the spins to align in the longitudinal direction is characterized by the T1 time constant [76]. Knowledge of the T1 time constant is useful for determining the ideal repetition rate between pulses to acquire the most signal in the shortest period of time. Electrons and electric currents in the material are also sources of magnetic moments. This means that the local magnetic field of each nucleus is unique and can have a slightly different magnitude and direction affecting the resonant frequency or rate of precession of the individual nucleus. These differences as well as field inhomogeneities result in the transverse magnetization induced by the radiofrequency wave slowly decaying away over time. This is called spin-spin

relaxation and is characterized by the T2 time constant. Spin-spin relaxation always accompanies spin-lattice relaxation. Equations describing the rate of relaxation are known as the Bloch equations [76].

Typically, the radiofrequency pulse length is chosen to maximize the signal in the transverse plane (called a 90° pulse). One pulse, followed by subsequent measurement is known as a Bloch decay since it follows the Bloch equations. Another common pulse sequence is a Hahn echo [77], which uses a refocussing pulse of 180° length. This creates a spin echo pulse some time after the FID, which is recorded instead of the FID.

Electrons have strong magnetic moments that affect the local magnetic field of the nucleus. Different chemical compounds will therefore have slightly different resonant frequencies due to their varying electronic configurations, and the amount that the principal components of the signal move in comparison to a reference is known as the chemical shift (δ), a feature which is defined in equation 3.4.

$$\delta = \frac{\omega_{\text{signal}} - \omega_{\text{ref}}}{\omega_{\text{spectrometer}}} \times 10^6 \quad (3.4)$$

The chemical shift may be exploited to determine what the electron bonding pattern is for materials being tested and to differentiate between different compounds. The electronic configuration is usually not spherically symmetric, so the chemical shift will change depending on the orientation of the molecule with the magnetic field. Since the molecules are typically oriented randomly, the signal will be a superposition of all of the possible alignments with the magnetic field. This shape is of interest to scientists who use the chemical shift anisotropy (CSA) to determine structural information for solids. The orientation of the molecule is not relevant for liquid samples since the molecular motions cause the anisotropy to average and a single isotropic peak is observed with no structural information gained. However, solids are more difficult to measure because of their short T₂ time. Since magnetic dipolar broadening from nearby nuclear spins is not averaged to zero by molecular motions, magnetic interactions between nuclei cause the FID to lose most of its intensity quite quickly [78]. Thus, pulses for T₂ excitation of solids are required to be shorter and more powerful which results in more heating due to the increased intensity of the radiowave.

One technique that can be used to sharpen the spectral peaks of a solid state sample is high frequency spinning at a certain angle which causes the dipolar interactions between nuclei to average to zero [79]. This

technique is known as magic angle spinning (MAS). In using MAS, structural information is traded for better resolution and sensitivity as higher frequency spinning results in sharper peaks [79]. Spinning of the sample produces peaks in the spectrum on either side of the isotropic peak, at a distance determined by the spin frequency [80]. These peaks are known as sidebands.

3.1.3 General Probe Design

A spectrometer setup includes: a magnet to supply an external field, an electronics interface plus computer, and an NMR probe. The NMR probe must be able to transmit and receive radiofrequency waves perpendicular to the main magnetic field at the resonant frequency. While the magnet and computer plus electronics remain the same between experiments, the probe is often re-configured depending on the experiment. The main components of the probe include: a radiofrequency (RF) coil (resonator), an RF power transmission line, and tuning/matching capacitors.

At its most basic, the RF coil is a RLC circuit with a given resistance (R), inductance (L) and capacitance (C). The resonant frequency ω of an RLC circuit occurs when the inductive and capacitive reactances are

of equal magnitude and the impedance of a circuit is purely real. This is given by

$$\omega = \frac{1}{\sqrt{LC}}. \quad (3.5)$$

If an alternating current is supplied to the circuit at a frequency which matches the resonant frequency, the circuit will oscillate with greater magnitude allowing the radiofrequency pulse to be applied. When receiving the signal, it is desirable to detect only frequencies within a certain bandwidth. The RLC circuit accomplishes this by acting as a bandpass filter to separate out undesired signals. The coil design is usually determined by the frequency, which is nuclide dependent, and the shape/size of the sample.

In between the power source and the RLC circuit is a cable. If the length of the cable is not significant in comparison to the wavelength of the transmitted signal or the length of the cable is an integer multiple of half the wavelength in the cable, the cable does not need to be considered in analysis and can be treated as a short circuit. If not, it must be treated as a transmission line and taken into account during analysis.

Before any measurements are taken, the coil must be tuned so that its resonant frequency matches that of the carrier frequency of the transmitted pulses and matched so that its impedance matches that of the transmission line. An impedance mismatch will cause reflections and insertion loss. This is necessary for each experiment as whichever experimental material is inside the coil will affect the tuning and matching of the circuit. The tuning and matching is performed by adjusting the values of two capacitors - one for matching, and one for tuning. It is an iterative process as changing the value of the tuning capacitor will affect the matching and changing the value of the matching capacitor will have an impact on the tuning. Other considerations when designing a probe include: ensuring there are no traces of the nuclide of interest in the probe body as contaminants would contribute to the measured signal and adding shielding to prevent background electromagnetic radiation from distorting the signal.

3.1.4 Fluorine NMR of Bone

Fluorine is a common element analyzed using NMR spectroscopy with its high gyromagnetic ratio, high isotopic abundance, and its unique binding properties. Fluorine NMR can be used to screen for the binding of ligands to

targets for potential drug development [81] and for probing protein structure and conformational changes [82]. As solids are difficult to perform NMR spectroscopy on, bone is a challenging location. NMR of bone has been done before using specialized pulse sequences with shorter pulses as well as MAS to analyze proton content [11, 83, 84], phosphorus content [11, 84, 85], as well as calcium and sodium content [86].

NMR measurement of fluorine in bone has not been studied extensively. The most thorough research into the subject was performed by a University of Toronto group between 1985 - 1995. They first analyzed ground rat bone samples with high fluorine levels [87]. This experiment yielded a detection limit of 9 mg F/g Ca in a 10 g sample. This same group also did *in vivo* work measuring human fingers [78]. This resulted in a detection limit of 1 mg F/cm length of bone (3 cm length of finger in coil). In theory, design improvements could be made to the setup through the use of: a) Magic Angle Spinning, b) better probe design, c) higher external magnetic fields, and d) more sample in the active volume. From this work, an idea of the potential fluorine signal in bone can be formed. Further human measurements have not occurred since then, however there has been research into fluorine NMR of similar compounds to human bone that might prove insightful.

Hydroxyapatite with differing amounts of fluoridation has been previously studied. Fluoridation is either reported in amount of hydroxyl substitution (100% substitution corresponding to pure fluorapatite), or in weight percentage (wt%) where 100% substitution corresponds to 3.77 wt%. Studies have shown that hydroxyfluorapatites ranging from 20–200% were all distinguishable from background [88] and that even apatites with 10% (0.4 wt%) substitution were distinguishable [89]. 10% hydroxyl substitution (0.4 wt%) would seem to be near the detection limit, as one study determined that a substitution of 0.4 wt% was not distinguishable from background, while a 0.83 wt% substitution was clearly distinguishable [90]. This discrepancy in detection limit is most likely due to the differences in experimental parameters such as rotor volume size between the two studies. Reporting of the experimental length was not documented in these studies, however one study found that 90% substitution, roughly 4% of the weight, of biomimetic mesocrystals was able to be detected with only 64 repetitions [91, 92].

Different chemical species in materials similar to human bone have been determined by MAS. A study analyzing fluoridation in shark teeth deconvolved the ^{19}F MAS signal to find fluorapatite (-102.6 ppm), hydroxyfluorapatite (-104.8 ppm), calcium fluoride (-108.7 ppm), and an

unknown peak (-74.2 ppm) [93]. The structure of biomimetic mesocrystals was analyzed by ^{19}F MAS and found to contain fluorapatite (-103 ppm), hydroxyfluorapatite (-104 ppm), and calcium fluoride (-108 ppm), as well as unknown compounds at -86 and -94 ppm [91]. Another study examined powdered teeth soaked in varying fluoride concentrations with ^{19}F MAS and found fluorapatite (-102 ppm) and calcium fluoride (-108 ppm) [94]. Static spectra of fine bone particles from rats exposed to 30 days of fluoride inhalation [95] were deconvolved to find phases belonging to F-apatite, CaF_2 , and what was hypothesized to be MgF_2 . The contribution to the signal from calcium fluoride results in an upfield hump in the isotropic peak of the analyzed sample.

All previous studies have indicated that the amount of fluoridation of the apatite affects the chemical shift range. Fully substituted apatite corresponds to a -102.6 ppm chemical shift, and as fluoride substitution decreases, the chemical shift becomes more negative. This relationship has been studied by Gao et al [88, 96], who found that decreasing fluoridation caused an exponential decay in chemical shift values. Some studies [90, 93, 94] also indicated an uneven CSA pattern in the spectra, providing insight into the expected shape of the signal. The spinning sideband with a lower chemical shift (referred to as upfield) was found to have a greater intensity

than the spinning sideband with a higher chemical shift (referred to as downfield).

Lower frequency spinning of apatite at 4.7 kHz [97] and shark teeth at 6 kHz [93] has shown a broader signal of roughly 100–150 ppm, while static spectra of fluoridated rat bones showed a span of ~ 250 ppm [95].

3.2 Methods

3.2.1 MAS Experiment

The first step in designing a biomedical NMR measuring system for fluorine was to perform MAS. It would be very difficult to perform MAS in an *in vivo* situation. However, the spinning makes the experiment more sensitive, and the data collected may be used to make predictions about the signal in an *in vivo* situation.

Magic angle spinning was performed at the McMaster NMR facility. A Bruker AV500 spectrometer with a built-in dead time of 4–5 μs was used along with a low-fluorine background probe. The sample rotor size was 4 mm, with an active volume of 125.33 mm³. Samples used in MAS

experiments are typically quite small and must be able to withstand being spun at very high speeds. Human skull pieces from the McMaster Anatomy Laboratory were provided as test materials. To get the pieces to fit inside the 4 mm rotor, they were first cut into small pieces using a dremmel saw, then crushed using a hydraulic laboratory press. This sample was spun at 5 kHz. There were some initial troubles bringing the sample up to the spinning speed, most likely due to the sample being unbalanced. A 4 μ s pulse with 126 watts of power was applied with a 0.3 s acquisition. Both Bloch decays and Hahn echoes were performed (20,480 scans each), but there was no measurable signal detected.

To try and get a signal, bone specimens were processed further into a powder. In powder form, it is possible to place more bone material in the rotor. Additionally, the rotor is more balanced which allows the sample to be spun at high frequencies more easily. To prepare the bone sample, cut bone pieces were ashed in a drying oven in a series of heating steps. The temperature and holding time lengths at each step are outlined in Table 3.1. The heating rates between heating steps were 2 °C/minute. Following the Environmental Protection Agency guidelines [98], these stepwise increases in heat ensure that moisture is removed, and charring done before ashing takes place. Previous work has shown that bone shows no significant

recrystallization or thermal decomposition at a temperature of 600°C [99–101], and that fluorine is not removed from the hydroxyapatite matrix until temperatures reach well over 1000°C [102,103]. A comparison of the first and second samples is shown in Figure 3.1

Temperature (°C)	Holding Time (min)
110	60
310	120
510	180
310	30
110	30
40	30

Table 3.1: Heating temperatures and holding times in oven to allow ashing of bone pieces. Ashing was done to make the sample more stable and compact when performing MAS.



Figure 3.1: Comparison of bone samples with different processing procedures. The ashed bone powder (a) was more stable than the crushed bone pieces (b) and able to spin at higher frequencies.

Additional fluoridated hydroxyapatite samples were prepared as they should have similar properties to bone, though have the potential to be made with high fluorine concentrations. These samples provide a good reference for any acquired signal from bone. Fluoridated hydroxyapatite samples were prepared by soaking hydroxyapatite powder in a 6000 ppm NaF

solution, followed by rinsing with distilled water over filter paper, and air drying for at least 12 hours. This follows similar work soaking apatite in fluorine solutions with subsequent filtering and drying [104,105].

Following similar procedures to the crushed bone sample experiment, 0.1 g of ashed bone powder was measured for 8192 scans, and 0.046 g of hydroxyapatite was measured for 256 scans. The samples were spun at 11 kHz, and spectra were collected over a 212 ppm spectral width. The pulse sequence was a standard 90° pulse with baseline subtraction using the *zgps* command in the Topspin library which is presented in Figure 3.2. The pulse sequence includes a 1.5 s relaxation delay D1, a 4 μ s 90° pulse, and two 8 μ s 180° pulses used to remove baseline signals. By using a square pulse, a broad frequency range will be excited as the fourier transform of a square wave results in a wide spectrum.

3.2.2 Bulk Sample Experiment

Based off the MAS work, the next step was to perform a static bulk sample measurement. Unfortunately, there was no ready-made probe capable of tuning to the frequency for fluorine at the NMR facility. To overcome this hurdle, a custom prototype probe was designed and fabricated. Another

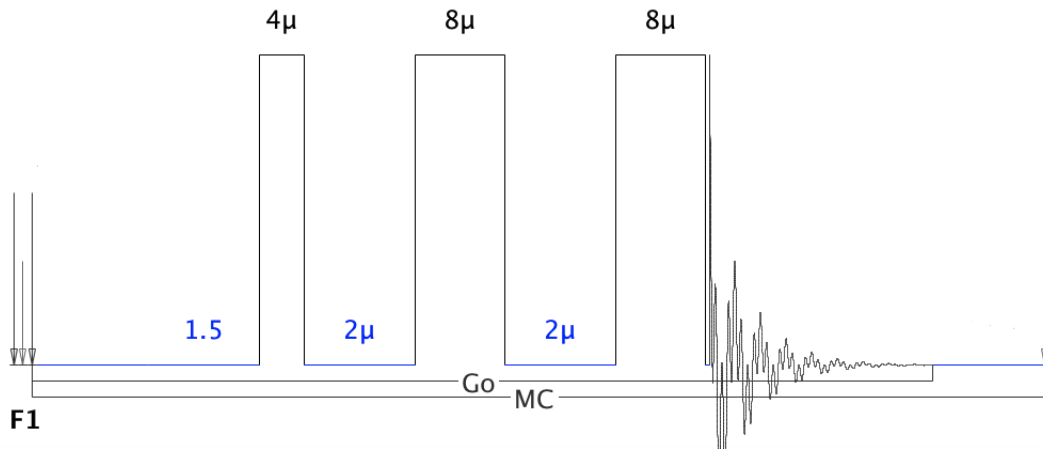


Figure 3.2: Pulse program used in Topspin to excite the bone sample and collect the FID. One 90° pulse was applied as well as two 180° refocussing pulses. The FID was then recorded. There was a 1.5 s relaxation delay between the end of data collection for an applied pulse and the start of a new excitation pulse.

custom probe would most likely have to be developed in future work to do human measurements, though the prototype probe is the first step toward making human *in vivo* measurements of bone fluorine possible.

The resonance coil used in the past was 14 turns of No. 26 wire, 3 cm in length, 2.3 cm diameter on a nylon surface [87]. NMR coils have upgraded since then where a common design used today is the birdcage coil. It is necessary for the probe to generate an even RF pulse within the sample of interest. This can be created in a cylinder with a z-directed surface

current, which is the design principle behind a birdcage coil [106] where sinusoidal currents are applied to each rung. Calculating the induction of the coil is complicated, which is why simplifications or a calculation tool are used.

The gyromagnetic ratio of fluorine is 40.052 MHz/T while the gyromagnetic ratio of hydrogen is 42.5775 MHz/T, so for a 200 MHz spectrometer, the required frequency for fluorine will be 188.137 MHz. For the RF coil, high Q capacitors are optimal. Following the work of Ref. [106], a birdcage coil was designed for larger samples. Using the birdcage builder app [107] [108], which has its interface shown in Figure 3.3, the capacitance value was calculated for this coil. The materials for the probe included: copper tape and copper wire, acrylic tubing, ceramic capacitors, and tin solder to ensure connections between the capacitors, legs, and end rings.

A coil which could fit into the in-house probe body containing shielding, tuning capacitors, and matching capacitors was designed. The birdcage builder app overestimated the capacitor value required, indicating that there was extra capacitance in the probe body. Using a value of 6.1 pF for each capacitor on the rungs, a resonant frequency of 227.5 MHz was found. Using a value of 11.1 pF, a resonant frequency of 188 MHz was found which is very close to fluorine's necessary frequency for a 200 MHz machine.

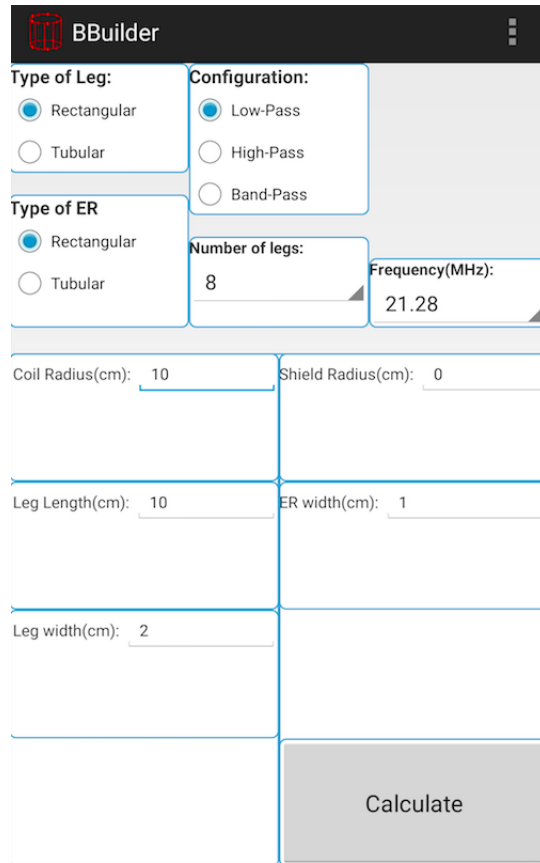


Figure 3.3: Birdcage builder app interface used to determine the required capacitance for each capacitor on the birdcage legs. Input values were estimated from the physical probe design.

Knowing the capacitor values that led to certain resonant frequencies, it was possible to back-calculate the extra capacitance in the probe which was determined to be 4.32 pF per leg. The input values to the birdcage builder app are shown in Table 3.2. The finished coil is presented in Figure 3.4 and its resonant peaks are shown in Figure 3.5.

App Input	Value
Type of Leg Configuration	Rectangular
Type of End Ring	Low-Pass
Number of Legs	Tubular
Coil Radius (cm)	8
Shield Radius (cm)	1.6
Leg Length (cm)	1.82
Leg Width (cm)	3.6
End Ring Inner Radius (cm)	0.65
End Ring Outer Radius (cm)	0
	0.05

Table 3.2: Final input values to the birdcage builder app resulting in capacitance values that agreed with experimental findings.

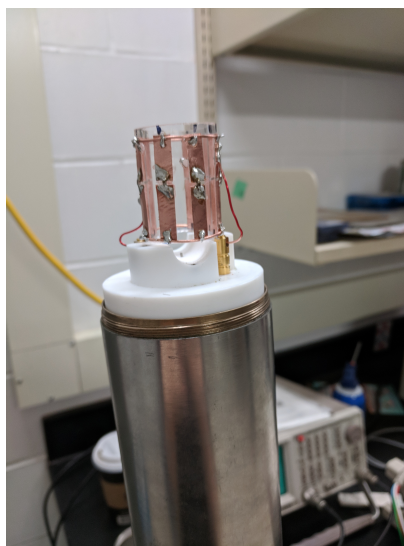


Figure 3.4: Prototype coil for measurement of bulk bone samples containing fluorine. The coil is shown with connections made to the probe body.

The coil was tested on the 200 MHz spectrometer at the McMaster NMR facility. The probe body and spectrometer setup are displayed in Figure 3.6. When performing testing, the phasing was changed to sharpen

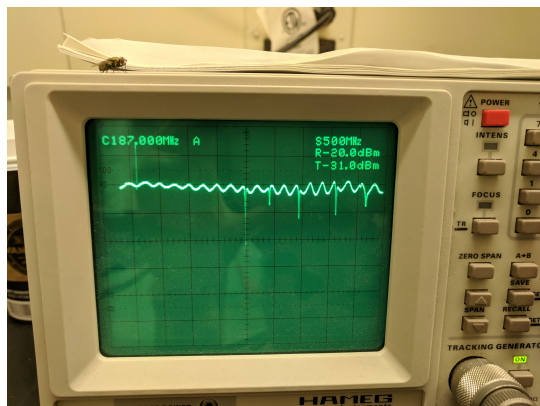


Figure 3.5: Resonant peaks of the prototype coil as displayed on a spectrum analyzer. The first peak corresponds to the desired resonant frequency of 188 MHz. The number of resonant peaks depends on the number of legs in the birdcage coil.

the signal, the pulse length was optimized to find the 90° pulse (*zg* command in Topspin), and the shims adjusted to narrow the signal. Tuning and matching was performed within the Bruker probe body. A high concentration sodium fluoride sample was used to test the coil. To ensure that the sample was in the middle of the volume, tissue was wrapped around it.

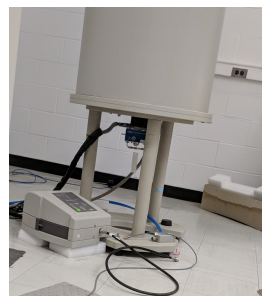
3.3 Results

3.3.1 MAS Experiment

The spectra were analyzed using the Topspin software [109]. The spectrum for the fluorohydroxyapatite sample is presented in Figure 3.7. The ashed



(a)



(b)

Figure 3.6: Experimental setup for testing of the prototype coil. The probe body used to make the measurements is displayed in (a), where the prototype coil can be seen attached on top. The matching and tuning adjustments are made with rods at the bottom of the probe body. The metal body provides shielding. The 200 MHz spectrometer that was used to perform testing is displayed in (b).

bone powder spectrum is shown in Figure 3.8. This spectrum was fit with the Solids Lineshape Analysis Tool in Topspin, including the hydrogen dipolar interaction, and is shown in Figure 3.9. A 74.6% overlap of the spectrum with the fit was observed, indicating good agreement according to the guidelines in the Topspin manual [110]. The span was calculated to be 122 ppm according to the Herzfeld-Berger convention [111]. A comparison of hydroxyapatite with the ashed powder spectrum is presented in Figure 3.10.

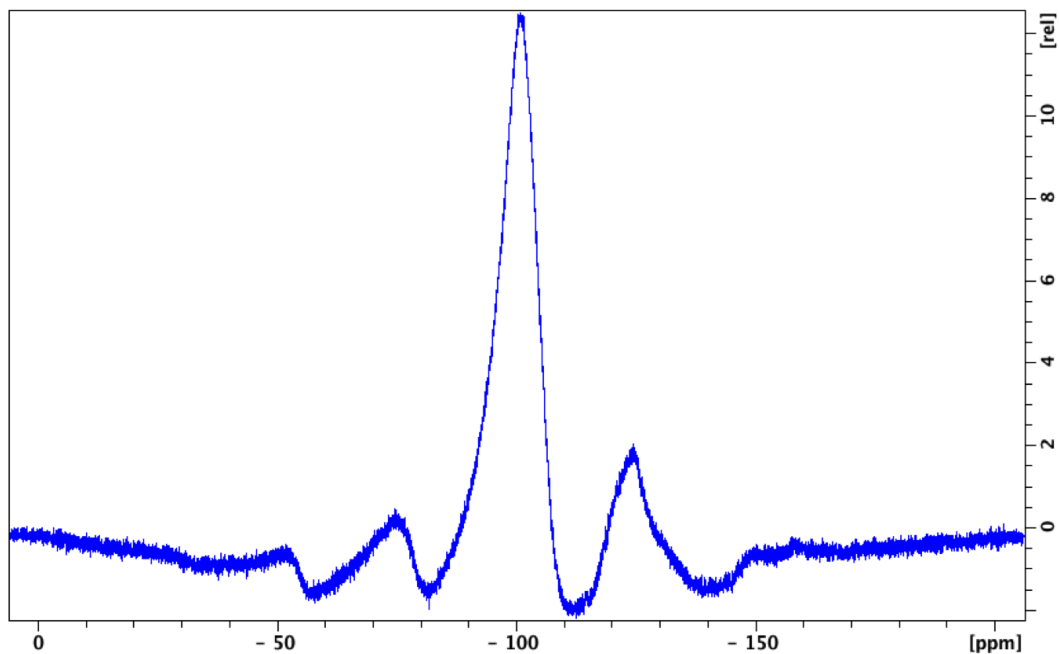


Figure 3.7: Spectrum of a 0.05 g fluoridated hydroxyapatite sample collected from a 11 kHz MAS experiment with 256 repetitions.

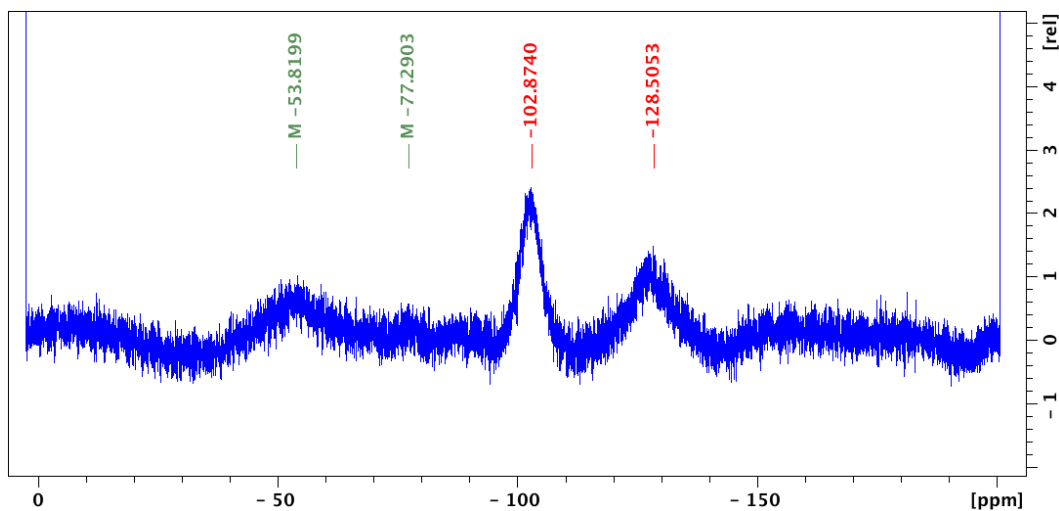


Figure 3.8: Spectrum of a 0.1 g ashed bone sample collected from a 11 kHz MAS experiment with 8192 repetitions.

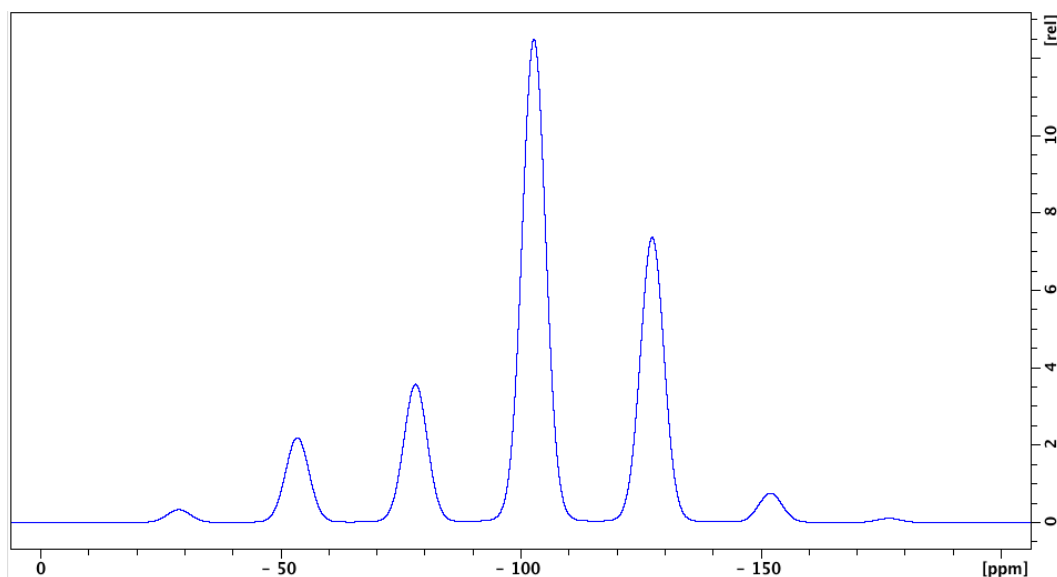


Figure 3.9: Fit to the ashed bone spectrum shown in Figure 3.8. The fit shows the placement of the spinning sidebands and the uneven distribution of signal intensity in the sidebands.

3.3.2 Bulk Sample Experiment

When testing the probe, the measurement signal was a broad peak with a long T1. With the original acrylic probe in the 200 MHz spectrometer, there was a broad signal (6 kHz) which had a 90° pulse length of 25 μ s. No change in signal was observed when a concentrated sodium fluoride solution was placed in the coil.

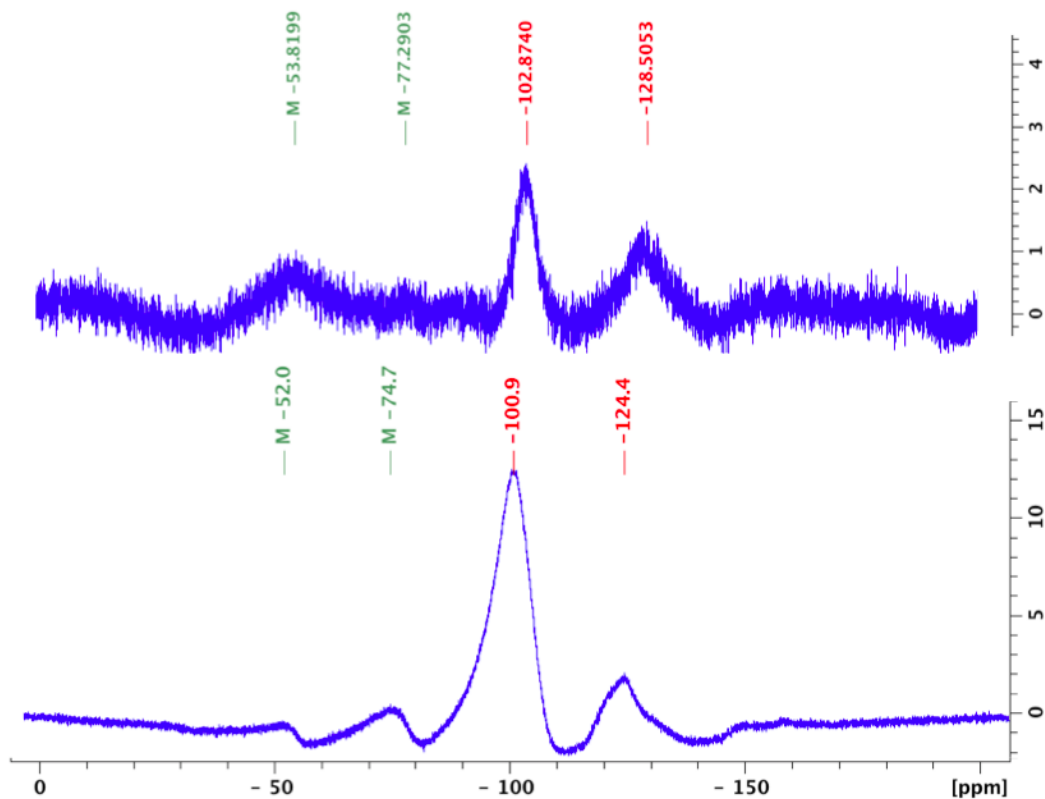


Figure 3.10: Comparison of chemical shift between the fluoridated hydroxyapatite spectrum and the ashed bone spectrum. The ashed bone spectrum has a more negative chemical shift. The sideband intensity pattern is similar in both spectra.

3.4 Discussion

Results from the MAS spectra collected from human bone samples showed a peak within the range corresponding to fluoridated hydroxyapatite. This measurement provides the first piece of evidence using ^{19}F NMR to classify human bone samples as containing fluoridated hydroxyapatite. The main peak of the ashed powder spectrum is shifted to the right of the

fluorohydroxyapatite peak which agrees with previous studies [88–91,94–96] as bone would not be expected to have complete substitution of fluorine. Both the fluoridated hydroxyapatite and ashed bone powder spectra have a CSA pattern that agrees with previous studies [90,93,94] as the upfield spinning sideband is of higher intensity than the downfield spinning sideband. Although it was suggested that fluorine in bone may be composed of multiple species including calcium fluoride [91,93,94], the isotropic peak of the ashed bone powder spectrum is symmetrical and does not appear to be composed of multiple chemical species. This could be due to the small signal. It could also be that calcium fluoride is only found in bone when fluorine levels are quite high, and there was no reason to anticipate higher-than-average levels of fluorine in this sample. Research into determining whether calcium fluoride is a marker of too much bone fluorine is a future consideration.

In the NMR community, the signal to noise ratio (SNR) is defined as the max peak height divided by the root-mean-square value of the noise [112]. The detection limit is determined based off of the SNR. The SNR of the main peak at -102.878 ppm in the ashed bone spectrum is 6.36. The region where the noise calculation was taken from was -91 to -96 ppm. This provides a good starting point on the expected signal when performing static measurements on bulk samples. In a static spectrum, the signal intensity

would be expected to be spread out over the calculated span of 122 ppm instead of localized into discretized peaks. Previous studies using slower spin speeds of 5–6 kHz also provide an estimate of the expected signal width. These studies had a span of roughly 100–150 ppm [93,97], while a static spectrum had a span of ~ 250 ppm [95]. It may be that the calculated span of the ashed bone spectrum should be bigger but the sideband peaks at further multiples of the spin frequency did not have a high enough intensity to be recognized by the fitting algorithm and included in the span calculation. The trade-off for a static measurement where the signal is now spread out over a much larger range with subsequent decreases in SNR, is that much more material can be measured.

The fluoridation studies described above provide a good idea on the amount of fluoride substitution that is detectable, a value which can be compared to the typical amounts of fluoride substitution in bone. To calculate the amount of bone that could reasonably be expected in a measurement, it is assumed that the index finger will be measured and that the total mass of the proximal phalange 2 will be in the active volume of the NMR coil. The proximal phalange 2 has a length of 39.4 ± 2.9 mm for males and 37.1 ± 3.7 mm for females according to a computed tomography study on hand bone samples [113]. Assuming a proximal phalange volume of 4 cm^3

based off a second metacarpal volume of approximately 7 cm^3 [113], there would be a cross sectional area of 1 cm^2 for a transverse slice through the finger or 4 cm^2 for a sagittal slice (which is where bone density measurements are taken). A typical bone mineral density (BMD) in the proximal phalanges is 0.6 g/cm^2 [114]. Multiplying the bone mineral density with the sagittal area, provides a value of 2.4 g. The total bone mineral mass in the phalanges has been estimated as 13 g [114], which is equivalent to 2.3 g per proximal phalange, which is consistent with our previous calculation.

With an estimate of the bone mineral mass that is expected in the active volume of the coil, the fluorine content in the active volume of the coil may also be calculated. Using the molar masses, the maximum weight contribution of fluorine, assuming complete replacement of the hydroxyl ion, is 3.76% or 0.06 g of fluorine. From previous work, the average fluorine concentration is 0.003 mg F/g Ca [62]. This is equivalent to 1 fluorine in bone apatite for every 30 hydroxyl ions or 0.15% of the bone mineral content being fluorine (3.4 mg). For comparison, Table 3.3 lists a comparison of the bone fluorine detection between different studies.

It is these estimates of the detection limit of ^{19}F NMR to detect fluoride in bone that prompted the building of a prototype probe to be used

Material	Material Amount	Magnet Strength (MHz)*	Spin Freq. (kHz)	Number of Aves	Amount Fluorine (mg)
Ground Rat Bone	7 g	27	0	1024	20
Human Finger	3 cm length	27	0	768	3
Hydroxyapatite	0.1 g	200	10	-	0.4
Biomimetic Mesocrystals	0.011 g	500	30	64	0.4
Ashed Bone (current work)	0.1 g	600	11	8192	0.15

Table 3.3: Comparison of approximate detection amounts of various experiments performing fluorine detection in bone or representative materials. *based on proton frequencies

for static measurements. Although there were difficulties in attaining a measurable signal from the probe, it is a good starting point for future *in vivo* designs. If a signal were to be successfully obtained, the next step would be to design a finger-simulating phantom to be used when optimizing parameters and determining detection limits. For an NMR phantom, interference from other elements due to activation as in NAA experiments is no longer a worry, since the resonant frequency is specifically tuned to fluorine (this frequency can be calculated for a specific magnetic strength using Equation 3.3). However, the way in which fluorine is bound will affect the signal. Thus the phantom design is completely different. A good representation would be hydroxyapatite doped with varying amounts of

fluorine and surrounded with an agarose gel to represent the detuning, power loss, and effect on T1 due to the soft tissue of the finger.

Minimizing the detection limit in any future setup must include optimization of the various parameters affecting the signal. Changing the magnetic field strength affects both the SNR as well as the resolution. Smaller magnetic fields result in finer resolution. On the 200 MHz machine (4.7 T), 1 ppm corresponds to 200 Hz, whereas on the 500 MHz machine (11.7 T), 1 ppm corresponds to 500 Hz. The SNR will be affected not only by the magnetic field strength (B_0) but also by the number of averages taken (t), and the number of nuclei being activated (n):

$$\text{SNR} \propto nB_0\sqrt{t}, \quad (3.6)$$

where n is the number of nuclei being activated, B_0 is the magnetic field strength, and t is the number of averages.

The relaxation constants T1 and T2 are properties that will affect the optimal pulse timing of future experiments. A T1 of 1.46 ± 0.07 s and a T2 of $75 \mu\text{s}$ has been found in previous work using a 27 MHz magnet [87]. However, T1 values for bone or apatite-like substances have a wide range of

reported values from 200 ms to 378 s [93, 115–118]. The pulse program used in the MAS experiment and outlined in Figure 3.2 provided a reasonable estimate to optimize the signal due to its pulse length being shorter than the T2, and relaxation delay being somewhere in the middle of the hypothesized T1 values (time it takes for 63% of the signal to recover). However, further optimization of the pulse timing could be done. Better estimates of the T1/T2 would also be helpful. Another consideration would be the volume of the sample/size of the coil. With increasing size, achieving a uniform radiofrequency wave as well as shimming becomes more difficult. The probe could be further optimized by driving the transmission in quadrature, making it more power efficient and increasing the SNR by a factor of $\sqrt{2}$ [106].

Future bone fluorine NMR work is not limited to *in vivo* situations, as analyzing the effects of different parameters would also give insight into bone's elemental metabolism. As bone is a highly substituted apatite, the concentrations of varying elemental substitutions may affect the signal. Strontium [119] and chlorine [120] have both been shown to affect ^{19}F MAS NMR spectra. As well, the location of the bone sample in the body may have some effect on its MAS spectrum. This initial experiment used skull samples due to its availability in the anatomy lab. Within the NMR field, there are also other techniques such as quantitative susceptibility mapping (QSM),

which analyzes the phase differences in signals caused by the susceptibility differences between compounds. Susceptibility differences are due to the strong magnetic fields of electrons which are responsible for the bulk magnetic properties of materials. QSM has had previous applications in iron determination [121] and classification of calcium salts in tissue [122]. Susceptibility differences of different compounds such as fluorohydroxyapatite and calcium fluoride could be measured with a susceptibility balance and compared with corresponding phase images. It is possible that different fluoride concentrations could affect the susceptibility measurements of bone. It is also possible that the differences are too small to measure and there are too many other bone substitutions with varying paramagnetic/diamagnetic properties obscuring the effect. Since susceptibility differences and chemical shifts are affected by the same parameters, comparisons between the two could be made. Overall, NMR could provide more information about the chemical structure of the material as well as its potential use as an *in vivo* measurement technique.

Chapter 4

Conclusion

Neutron activation analysis and nuclear magnetic resonance represent the only ways of directly measuring bone fluorine *in vivo*. From the MAS experiment, there is confirmation that fluoride is indeed binding to bone apatite, though other chemical species have yet to be determined. Currently, NAA remains the best technique for *in vivo* determination in that a functioning system exists with a known MDL. However, this research has shown that the previously calculated MDL may not be quite accurate and the technique not quite as sensitive as earlier determined. The NMR technique shows promise as a tool to examine bonding structure in bone through advanced analysis of samples. However, as an *in vivo* technique,

further work is needed to optimize the probe to lower its detection limit to be within the same range as the NAA technique. If it could, measurement of groups of people using both techniques to determine agreement between the two methods would be possible.

There are trade-offs associated with each technique. The NAA method provides instantaneous information on the other elemental concentrations in the hand, which means that the ratio of fluorine to other elements can be determined. Determining the relative amount of fluorine as opposed to the absolute amount of fluorine is now possible, as the concentration of elements such as calcium and sodium provide information regarding the amount of bone being measured. It may be that the relative concentration of fluorine is a more important measure of bone health as opposed to the total amount of fluorine. As phosphorus comprises part of hydroxyapatite, the fluorine NMR signal could be compared to a phosphorus NMR signal as phosphorus-31 is NMR-active. However, sequential measurements would have to be taken and another probe designed to resonate at the Larmor frequency of phosphorus. The ability of NAA to provide other elemental information comes at a cost, as these other elements have the potential to obscure the collected signal of interest. This is not the case in NMR where each NMR-active nucleus has a specific resonant

frequency at which a radiofrequency pulse will be applied. NAA is a radioactive technique, conferring radiation dose to the participants. This means that any time it is performed, a radioactive work permit must be approved. As well, the radiation dose sets an upper limit on the strength of the applied neutron field. NMR has no ionizing radiation, and safety considerations are limited to general magnet safety as well as possible heating due to the radiofrequency pulse. It may also be easier to convince research participants to take part in a study involving procedures "similar to a Magnetic Resonance Imaging (MRI) scan" as opposed to radioactive procedures. It's also possible that the NMR technique could have a more widespread availability if it could be used with MRI setups or even smaller portable magnets, while NAA is a technique limited to highly-focussed, intense neutron fields.

It may be that these techniques are complementary. Both of these methods provide unique information that may be useful in different scenarios. For example, NMR may prove a good tool as a quick diagnostic technique to determine fluorine amounts, especially in cases of potentially high contamination, while NAA remains a technique with high sensitivity to separate out how various factors and activities may affect fluoride accumulation.

Future research studies of *in vivo* fluoride measurement may be directed at examining the optimal levels of fluoride in people suffering from osteoporosis or the differences in fluoride accumulation between trabecular and cortical regions. As so many pharmaceuticals contain fluorine, *in vivo* measurements of people treated with fluorine-containing drugs would determine how their usage impacts bone fluoride levels. These are just a few of the areas that are still waiting to be studied, and there are still many questions to be answered as to the intricacies and impact of fluoride in bone.

Bibliography

- [1] K. Muller, C. Faeh, and F. Diederich, “Fluorine in Pharmaceuticals: Looking Beyond Intuition,” *Science*, vol. 317, pp. 1881–1886, Sept. 2007.
- [2] J. Wang, M. Sánchez-Roselló, J. L. Aceña, C. del Pozo, A. E. Sorochinsky, S. Fustero, V. A. Soloshonok, and H. Liu, “Fluorine in Pharmaceutical Industry: Fluorine-Containing Drugs Introduced to the Market in the Last Decade (2001–2011),” *Chemical Reviews*, vol. 114, pp. 2432–2506, Feb. 2014.
- [3] H. J. M. Bowen, “Environmental chemistry of the elements,” 1979.
- [4] W. R. Dolbier, *Guide to Fluorine Nuclear Magnetic Resonance for Organic Chemists*. John Wiley & Sons, Ltd, 2 ed., 2016.

- [5] H. Chen, M. Yan, X. Yang, Z. Chen, G. Wang, D. Schmidt-Vogt, Y. Xu, and J. Xu, “Spatial distribution and temporal variation of high fluoride contents in groundwater and prevalence of fluorosis in humans in Yuanmou County, Southwest China,” *Journal of Hazardous Materials*, vol. 235-236, pp. 201–209, Oct. 2012.
- [6] S. K. Jha, V. K. Mishra, D. K. Sharma, and T. Damodaran, “Fluoride in the environment and its metabolism in humans,” in *Reviews of Environmental Contamination and Toxicology Volume 211*, pp. 121–142, Springer, 2011.
- [7] F. E. McNeill, F. Mostafaei, A. Pidruczny, and D. R. Chettle, “Correlation between fluorine content in tea and bone assessed using neutron activation analysis in a Canadian urban population,” *Journal of Radioanalytical and Nuclear Chemistry*, vol. 309, pp. 389–395, July 2016.
- [8] W. Snyder, M. Cook, E. Nasset, L. Karhausen, G. Howells, and I. Tipton, “Report of the Task Group on Reference Man,” tech. rep., Pergamon Press, Oct. 1974.
- [9] N. Medellin-Castillo, R. Leyva-Ramos, E. Padilla-Ortega, R. O. Perez, J. Flores-Cano, and M. Berber-Mendoza, “Adsorption capacity of bone

- char for removing fluoride from water solution. Role of hydroxyapatite content, adsorption mechanism and competing anions,” *Journal of Industrial and Engineering Chemistry*, vol. 20, pp. 4014–4021, Nov. 2014.
- [10] Y. Nie, C. Hu, and C. Kong, “Enhanced fluoride adsorption using Al (III) modified calcium hydroxyapatite,” *Journal of Hazardous Materials*, vol. 233-234, pp. 194–199, Sept. 2012.
- [11] G. Cho, “Detection of Hydroxyl Ions in Bone Mineral by Solid-State NMR Spectroscopy,” *Science*, vol. 300, pp. 1123–1127, May 2003.
- [12] C. H. Turner, G. Boivin, and P. J. Meunier, “A mathematical model for fluoride uptake by the skeleton,” *Calcified Tissue International*, vol. 52, pp. 130–138, Feb. 1993.
- [13] G. Whitford, “Intake and Metabolism of Fluoride,” *Advances in Dental Research*, vol. 8, pp. 5–14, June 1994.
- [14] M. Scarpa, F. Vianello, A. Rigo, P. Viglino, F. Bracco, and L. Battistin, “Uptake and life time of fluoride ion in rats by ^{19}F -NMR,” *Magnetic Resonance Imaging*, vol. 11, pp. 697–703, Jan. 1993.
- [15] P. E. Petersen and M. A. Lennon, “Effective use of fluorides for the prevention of dental caries in the 21st century: The WHO approach,”

- Community Dentistry and Oral Epidemiology*, vol. 32, pp. 319–321, Oct. 2004.
- [16] F. M. Fordyce, K. Vrana, E. Zhovinsky, V. Povoroznuk, G. Toth, B. C. Hope, U. Iljinsky, and J. Baker, “A health risk assessment for fluoride in Central Europe,” *Environmental Geochemistry and Health*, vol. 29, pp. 83–102, Mar. 2007.
- [17] R. Balena, M. Kleerekoper, J. A. Foldes, M.-S. Shih, D. Sudhaker Rao, H. C. Schober, and A. M. Parfitt, “Effects of Different Regimens of Sodium Fluoride Treatment for Osteoporosis on the Structure, Remodeling and Mineralization of Bone,” *Osteoporosis International*, vol. 8, pp. 428–435, Aug. 1998.
- [18] E. Rokita, P. H. A. Mutsaers, J. A. Quaedackers, and G. Taton, “Bone mineralization after strontium and fluoride treatment in osteoporosis,” p. 6, 1999.
- [19] M. H. Lafage, R. Balena, M. A. Battle, M. Shea, J. G. Sedor, H. Klein, W. C. Hayes, and G. A. Rodan, “Comparison of alendronate and sodium fluoride effects on cancellous and cortical bone in minipigs. A one-year study,” *Journal of Clinical Investigation*, vol. 95, no. 5, p. 2127, 1995.

- [20] P. Vestergaard, N. R. Jorgensen, P. Schwarz, and L. Mosekilde, "Effects of treatment with fluoride on bone mineral density and fracture risk - a meta-analysis," *Osteoporosis International*, vol. 19, pp. 257–268, Mar. 2008.
- [21] D. Chachra, H. Limeback, T. Willett, and M. Grynopas, "The Long-term Effects of Water Fluoridation on the Human Skeleton," *Journal of Dental Research*, vol. 89, pp. 1219–1223, Nov. 2010.
- [22] R. Lehmann, M. Wapniarz, B. Hofmann, B. Pieper, I. Haubitz, and B. Alolio, "Drinking water fluoridation: Bone mineral density and hip fracture incidence," *Bone*, vol. 22, no. 3, pp. 273–278, 1998.
- [23] J. A. Cauley, A. M. Buhari, P. A. Murphy, and T. J. Riley, "Effects of fluoridated drinking water on bone mass and fractures: The study of osteoporotic fractures," *Journal of bone and mineral research*, vol. 10, no. 7, pp. 1076–1086, 1995.
- [24] B. Alolio and R. Lehmann, "Drinking water fluoridation and bone," *Experimental and Clinical Endocrinology & Diabetes*, vol. 107, pp. 12–20, July 2009.
- [25] A. G. Pereira, F. Y. Chiba, M. S. de Lima Coutinho Mattera, R. F. Pereira, R. de Cássia Alves Nunes, T. V. S. Tsosura, R. Okamoto, and

- D. H. Sumida, “Effects of fluoride on insulin signaling and bone metabolism in ovariectomized rats,” *Journal of Trace Elements in Medicine and Biology*, vol. 39, pp. 140–146, Jan. 2017.
- [26] B. L. Fina, M. Lupo, E. R. Da Ros, M. Lombarte, and A. Rigalli, “Bone Strength in Growing Rats Treated with Fluoride: A Multi-dose Histomorphometric, Biomechanical and Densitometric Study,” *Biological Trace Element Research*, Feb. 2018.
- [27] S. Nawata, T. Kaneta, M. Ogawa, Y. Ishiwata, N. Kobayashi, A. Shishikura-Hino, K. Yoshida, Y. Inaba, T. Saito, and T. Inoue, “Differences in sodium fluoride-18 uptake in the normal skeleton depending on the location and characteristics of the bone,” *Nuklearmedizin*, vol. 56, no. 03, pp. 91–96, 2017.
- [28] P. Santhanam, S. P. Rowe, L. B. Solnes, and M. S. Javadi, “Plasma Fluoride Level and Femoral Bone Mineral Density in Post-Menopausal Women,” *The International Journal of Occupational and Environmental Medicine*, vol. 8, pp. 56–57, Jan. 2017.
- [29] C. Riedel, E. A. Zimmermann, J. Zustin, M. Niece, M. Amling, M. Grynpas, and B. Busse, “The incorporation of fluoride and strontium in hydroxyapatite affects the composition, structure, and

- mechanical properties of human cortical bone: EFFECTS OF FLUORIDE AND STRONTIUM ON HUMAN BONE QUALITY,” *Journal of Biomedical Materials Research Part A*, vol. 105, pp. 433–442, Feb. 2017.
- [30] L. Chai, H. Wang, H. Zhao, and S. Dong, “Chronic Effects of Fluoride Exposure on Growth, Metamorphosis, and Skeleton Development in *Bufo gargarizans* Larvae,” *Bulletin of Environmental Contamination and Toxicology*, vol. 98, pp. 496–501, Apr. 2017.
- [31] V. Interlandi, P. A. Fontanetti, R. H. Ponce, R. V. Gallará, and V. A. Centeno, “Chronic Exposure to Fluoride During Gestation and Lactation Increases Mandibular Bone Volume of Suckling Rats,” *Biological Trace Element Research*, Feb. 2018.
- [32] E. Everett, “Fluoride’s Effects on the Formation of Teeth and Bones, and the Influence of Genetics,” *Journal of Dental Research*, vol. 90, pp. 552–560, May 2011.
- [33] M. Dermience, G. Lognay, F. Mathieu, and P. Goyens, “Effects of thirty elements on bone metabolism,” *Journal of Trace Elements in Medicine and Biology*, vol. 32, pp. 86–106, Oct. 2015.

- [34] J. Pei, B. Li, Y. Gao, Y. Wei, L. Zhou, H. Yao, J. Wang, and D. Sun, “Fluoride decreased osteoclastic bone resorption through the inhibition of NFATc1 gene expression: Fluoride Decreased Osteoclastic Bone Resorption,” *Environmental Toxicology*, vol. 29, pp. 588–595, May 2014.
- [35] W.-J. Qu, D.-B. Zhong, P.-F. Wu, J.-F. Wang, and B. Han, “Sodium fluoride modulates caprine osteoblast proliferation and differentiation,” *Journal of Bone and Mineral Metabolism*, vol. 26, pp. 328–334, July 2008.
- [36] D. Gandhi, P. K. Naoghare, A. Bafana, K. Kannan, and S. Sivanesan, “Fluoride-Induced Oxidative and Inflammatory Stress in Osteosarcoma Cells: Does It Affect Bone Development Pathway?,” *Biological Trace Element Research*, vol. 175, pp. 103–111, Jan. 2017.
- [37] A. P. Daiwile, S. Sivanesan, P. Tarale, P. K. Naoghare, A. Bafana, D. Parmar, and K. Kannan, “Role of fluoride induced histone trimethylation in development of skeletal fluorosis,” *Environmental Toxicology and Pharmacology*, vol. 57, pp. 159–165, Jan. 2018.
- [38] C. H. Turner, L. P. Garetto, A. J. Dunipace, W. Zhang, M. E. Wilson, M. D. Grynpas, D. Chachra, R. McClintock, M. Peacock, and G. K. Stookey, “Fluoride Treatment Increased Serum IGF-1, Bone Turnover,

- and Bone Mass, but Not Bone Strength, in Rabbits,” *Calcified Tissue International*, vol. 61, pp. 77–83, July 1997.
- [39] Z. Zhou, H. Wang, B. Zheng, Z. Han, Y. Chen, and Y. Ma, “A Rat Experimental Study of the Relationship Between Fluoride Exposure and Sensitive Biomarkers,” *Biological Trace Element Research*, vol. 180, pp. 100–109, Nov. 2017.
- [40] S. Proksch, J. Brossart, K. Vach, E. Hellwig, M. J. Altenburger, and L. Karygianni, “Evaluation of the bioactivity of fluoride-enriched mineral trioxide aggregate on osteoblasts,” *International Endodontic Journal*, Feb. 2018.
- [41] G. Ren, K. Wang, R. Chang, Y. Su, J. Wang, J. Su, and B. Han, “Simultaneous Administration of Fluoride and Selenite Regulates Proliferation and Apoptosis in Murine Osteoblast-like MC3T3-E1 Cells by Altering Osteoprotegerin,” *Biological Trace Element Research*, vol. 144, pp. 1437–1448, Dec. 2011.
- [42] J. H. Shepherd, D. V. Shepherd, and S. M. Best, “Substituted hydroxyapatites for bone repair,” *Journal of Materials Science: Materials in Medicine*, vol. 23, pp. 2335–2347, Oct. 2012.

- [43] Y. Suzuki, "The normal levels of fluorine in the bone tissue of Japanese subjects.," *The Tohoku Journal of Experimental Medicine*, vol. 129, no. 4, pp. 327–336, 1979.
- [44] V. Zaichick, "Chemical Elements of Human Bone Tissue Investigated by Nuclear Analytical and Related Methods," *Biological Trace Element Research*, vol. 153, pp. 84–99, June 2013.
- [45] C. S. Sastri, V. Iyengar, G. Blondiaux, Y. Tessier, H. Petri, P. Hoffmann, N. K. Aras, V. Zaichick, and H. M. Ortner, "Fluorine determination in human and animal bones by particle-induced gamma-ray emission," *Fresenius' Journal of Analytical Chemistry*, vol. 370, pp. 924–929, Aug. 2001.
- [46] D. L. Samudralwar and J. D. Robertson, "Determination of major and trace elements in bones by simultaneous PIXE/PIGE analysis," *Journal of Radioanalytical and Nuclear Chemistry Articles*, vol. 169, pp. 259–267, Mar. 1993.
- [47] D. R. Tilley, C. M. Cheves, J. H. Kelley, S. Raman, and H. R. Weller, "Energy Levels of Light Nuclei," p. 153.
- [48] A. Pejović-Milić, S. H. Byun, D. R. Chettle, F. E. McNeill, and W. V. Prestwich, "Development of an irradiation/shielding cavity for in vivo

- neutron activation analysis of manganese in human bone,” *Journal of Radioanalytical and Nuclear Chemistry*, vol. 269, pp. 417–420, Aug. 2006.
- [49] W. Matysiak, J. Atanackovic, H. Katalmohseni, S. Byun, M. Inskip, W. Prestwich, N. Priest, K. Chin, D. Cowan, and D. Chettle, “In-Vivo Neutron Activation Analysis for Aluminium in Bone: System Upgrade and Improve Data Analysis,” *AECL Nuclear Review*, vol. 2, pp. 27–32, Dec. 2013.
- [50] K. Davis, Aslam, A. Pejović-Milić, and D. R. Chettle, “*In Vivo* measurement of bone aluminum in population living in southern Ontario, Canada: *In vivo* measurement of bone aluminum,” *Medical Physics*, vol. 35, pp. 5115–5123, Oct. 2008.
- [51] M. L. Arnold, F. E. McNeill, I. M. Stronach, A. Pejovic-Milic, D. R. Chettle, and A. Waker, “An accelerator based system for *in vivo* neutron activation analysis measurements of manganese in human hand bones,” *Medical Physics*, vol. 29, pp. 2718–2724, Oct. 2002.
- [52] A. Pejović-Milić, D. R. Chettle, and F. E. McNeill, “Quantification of manganese in human hand bones: A feasibility study,” *Physics in Medicine and Biology*, vol. 53, pp. 4081–4092, Aug. 2008.

- [53] A. Pejović-Milić, M. Arnold, F. McNeill, and D. Chettle, “Monte Carlo design study for in vivo bone aluminum measurement using a low energy accelerator beam,” *Applied Radiation and Isotopes*, vol. 53, pp. 657–664, Nov. 2000.
- [54] M. Chamberlain, J. L. Gräfe, S. H. Byun, D. R. Chettle, L. M. Egden, G. M. Orchard, C. E. Webber, and F. E. McNeill, “The feasibility of *in vivo* quantification of bone-fluorine in humans by delayed neutron activation analysis: A pilot study,” *Physiological Measurement*, vol. 33, pp. 243–257, Feb. 2012.
- [55] F. Mostafaei, F. E. McNeill, D. R. Chettle, and W. V. Prestwich, “Improvements in an *in vivo* neutron activation analysis (NAA) method for the measurement of fluorine in human bone,” *Physiological Measurement*, vol. 34, pp. 1329–1341, Oct. 2013.
- [56] M. Chamberlain, J. L. Gräfe, Aslam, S.-H. Byun, D. R. Chettle, L. M. Egden, C. E. Webber, and F. E. McNeill, “*In Vivo* quantification of bone-fluorine by delayed neutron activation analysis: A pilot study of hand-bone-fluorine levels in a Canadian population,” *Physiological Measurement*, vol. 33, pp. 375–384, Mar. 2012.

- [57] S. Byun, W. Prestwich, K. Chin, F. McNeill, and D. Chettle, “Efficiency calibration and coincidence summing correction for a 4π NaI(Tl) detector array,” *Nuclear Instruments and Methods in Physics Research Section A: Accelerators, Spectrometers, Detectors and Associated Equipment*, vol. 535, pp. 674–685, Dec. 2004.
- [58] S. Byun, W. Prestwich, K. Chin, F. McNeill, and D. Chettle, “ 4π NaI(Tl) Detector Array for In Vivo Neutron Activation Analysis,” *IEEE Transactions on Nuclear Science*, vol. 53, pp. 2944–2947, Oct. 2006.
- [59] J. A. Cooper, “Factors determining the ultimate detection sensitivity of Ge (Li) gamma-ray spectrometers,” *Nuclear Instruments and Methods*, vol. 82, pp. 273–277, 1970.
- [60] G. F. Knoll, “Radiation detection and measurement / Glenn F. Knoll.,” 2010.
- [61] F. Mostafaei, F. E. McNeill, D. R. Chettle, W. V. Prestwich, and M. Inskip, “Design of a phantom equivalent to measure bone-fluorine in a human’s hand via delayed neutron activation analysis,” *Physiological Measurement*, vol. 34, pp. 503–512, May 2013.

- [62] F. Mostafaei, F. E. McNeill, D. R. Chettle, W. V. Prestwich, and M. Inskip, “Design of a phantom equivalent to measure bone-fluorine in a human’s hand via delayed neutron activation analysis,” *Physiological Measurement*, vol. 34, pp. 503–512, May 2013.
- [63] S. Byun, K. Chin, W. Prestwich, F. McNeill, and D. Chettle, “A DSP-based multichannel analyzer for simultaneous acquisition of coincidence and anticoincidence spectra,” *Nuclear Instruments and Methods in Physics Research Section B: Beam Interactions with Materials and Atoms*, vol. 263, pp. 116–118, Oct. 2007.
- [64] J. Gräfe, F. McNeill, S. Byun, D. Chettle, and M. Noseworthy, “The feasibility of in vivo detection of gadolinium by prompt gamma neutron activation analysis following gadolinium-based contrast-enhanced MRI,” *Applied Radiation and Isotopes*, vol. 69, pp. 105–111, Jan. 2011.
- [65] S. H. Byun, A. Pejović-Milić, S. McMaster, W. Matysiak, Aslam, Z. Liu, L. M. Watters, W. V. Prestwich, F. E. McNeill, and D. R. Chettle, “Dosimetric characterization of the irradiation cavity for accelerator-based *in vivo* neutron activation analysis,” *Physics in Medicine and Biology*, vol. 52, pp. 1693–1703, Mar. 2007.

- [66] “Definition and Procedure for the Determination of the Method Detection Limit,” Tech. Rep. 2, United States Environmental Protection Agency, Dec. 2016.
- [67] L. A. Currie, “Limits for qualitative detection and quantitative determination. Application to radiochemistry,” *Analytical chemistry*, vol. 40, no. 3, pp. 586–593, 1968.
- [68] P. R. Bevington, 1933, “Data reduction and error analysis for the physical sciences / Philip R. Bevington, D. Keith Robinson.,” 2003.
- [69] M. Lord, F. McNeill, J. Gräfe, M. Noseworthy, and D. Chettle, “A phantom-based feasibility study for detection of gadolinium in bone in-vivo using X-ray fluorescence,” *Applied Radiation and Isotopes*, vol. 112, pp. 103–109, June 2016.
- [70] D. Comsa, W. Prestwich, F. McNeill, and S. Byun, “Application of spectral decomposition analysis to in vivo quantification of aluminum by neutron activation analysis,” *Applied Radiation and Isotopes*, vol. 61, pp. 1353–1360, Dec. 2004.
- [71] H. K. Mohseni, “IN VIVO MEASUREMENT OF BONE ALUMINUM IN ALZHEIMER’S DISEASE AND RELATED STUDIES,” *Medical Physics*, p. 225.

- [72] A. Bohr and B. R. Mottelson, “BETA-DECAY AND THE SHELL MODEL, AND THE INFLUENCE OF COLLECTIVE MOTION ON NUCLEAR TRANSITIONS \sim *),” p. 13.
- [73] M. H. Levitt, “Spin Dynamics : Basics of Nuclear Magnetic Resonance. [electronic resource],” 2008.
- [74] L. G. Hanson, “Is quantum mechanics necessary for understanding magnetic resonance?,” *Concepts in Magnetic Resonance Part A*, vol. 32A, pp. 329–340, Sept. 2008.
- [75] M. Goldman, “Formal Theory of Spin–Lattice Relaxation,” *Journal of Magnetic Resonance*, vol. 149, pp. 160–187, Apr. 2001.
- [76] F. Bloch, “Nuclear Induction,” *Physical Review*, vol. 70, Oct. 1946.
- [77] E. L. Hahn, “Spin Echoes,” *Physical Review*, vol. 80, pp. 580–594, Nov. 1950.
- [78] M. E. Ebifegha, R. F. Code, J. E. Harrison, K. G. McNeill, and M. Szyjkowski, “In vivo analysis of bone fluoride content via NMR,” *Physics in Medicine and Biology*, vol. 32, pp. 439–451, Apr. 1987.
- [79] I. Lowe, “Free Induction Decays of Rotating Solids,” *Physical Review Letters*, vol. 2, no. 7, p. 3, 1959.

- [80] M. Maricq and J. S. Waugh, "NMR in rotating solids," *The Journal of Chemical Physics*, vol. 70, pp. 3300–3316, Apr. 1979.
- [81] C. Dalvit, P. E. Fagerness, D. T. A. Hadden, R. W. Sarver, and B. J. Stockman, "Fluorine-NMR Experiments for High-Throughput Screening: Theoretical Aspects, Practical Considerations, and Range of Applicability," *Journal of the American Chemical Society*, vol. 125, pp. 7696–7703, June 2003.
- [82] M. A. Danielson and J. J. Falke, "Use of ^{19}F NMR to Probe Protein Structure and Conformational Changes," p. 35.
- [83] J. Du and G. M. Bydder, "Qualitative and quantitative ultrashort-TE MRI of cortical bone: QUALITATIVE AND QUANTITATIVE BONE IMAGING," *NMR in Biomedicine*, vol. 26, pp. 489–506, May 2013.
- [84] Y. Wu, D. A. Chesler, M. J. Glimcher, L. Garrido, J. Wang, H. J. Jiang, and J. L. Ackerman, "Multinuclear solid-state three-dimensional MRI of bone and synthetic calcium phosphates," *Proceedings of the National Academy of Sciences*, vol. 96, pp. 1574–1578, Feb. 1999.
- [85] E. Brown and J. H. Battoclettl, "In Vivo ^{31}P Nuclear Magnetic Resonance Spectroscopy of Bone Mineral for Evaluation of Osteoporosis," p. 8.

- [86] D. Laurencin, A. Wong, W. Chrzanowski, J. C. Knowles, D. Qiu, D. M. Pickup, R. J. Newport, Z. Gan, M. J. Duer, and M. E. Smith, “Probing the calcium and sodium local environment in bones and teeth using multinuclear solid state NMR and X-ray absorption spectroscopy,” *Phys. Chem. Chem. Phys.*, vol. 12, no. 5, pp. 1081–1091, 2010.
- [87] M. E. Ebifegha, R. F. Code, K. G. McNeill, and M. Szyjkowski, “Nuclear-magnetic-resonance determinations of fluorine content and relaxation times in bone powder,” *Canadian Journal of Physics*, vol. 64, pp. 282–288, Mar. 1986.
- [88] Y. Gao, N. Karpukhina, and R. V. Law, “Phase segregation in hydroxyfluorapatite solid solution at high temperatures studied by combined XRD/solid state NMR,” *RSC Adv.*, vol. 6, no. 105, pp. 103782–103790, 2016.
- [89] M. O’Donnell, R. Hill, R. Law, and S. Fong, “Raman spectroscopy, ^{19}F and ^{31}P MAS-NMR of a series of fluorochloroapatites,” *Journal of the European Ceramic Society*, vol. 29, pp. 377–384, Feb. 2009.
- [90] J. Chen, Z. Yu, P. Zhu, J. Wang, Z. Gan, J. Wei, Y. Zhao, and S. Wei, “Effects of fluorine on the structure of fluorohydroxyapatite: A study

- by XRD, solid-state NMR and Raman spectroscopy,” *Journal of Materials Chemistry B*, vol. 3, no. 1, pp. 34–38, 2015.
- [91] A. Vyalikh, P. Simon, E. Rosseeva, J. Buder, U. Scheler, and R. Kniep, “An NMR Study of Biomimetic Fluorapatite – Gelatine Mesocrystals,” *Scientific Reports*, vol. 5, p. 15797, Oct. 2015.
- [92] S. Busch, U. Schwartz, and R. Kniep, “Chemical and Structural Investigations of Biomimetically Grown Fluorapatite-Gelatin Composite Aggregates,” *Advanced Functional Materials*, 2003.
- [93] H.-H. Chang, M.-J. Chien, C.-C. Kao, Y.-J. Chao, P.-T. Yu, C.-Y. Chang, S.-J. Huang, Y.-L. Lee, and J. C. C. Chan, “Structural Characterization of Fluoride Species in Shark Teeth,” *Chem. Commun.*, 2017.
- [94] N. Mohammed, N. Kent, R. Lynch, N. Karpukhina, R. Hill, and P. Anderson, “Effects of Fluoride on in vitro Enamel Demineralization Analyzed by ^{19}F MAS-NMR,” *Caries Research*, vol. 47, no. 5, pp. 421–428, 2013.
- [95] S. P. Gabuda, A. A. Gaidash, S. G. Kozlova, and N. L. Allan, “Structural forms of fluorides in bone tissue of animals under chronic

- fluoride intoxication,” *Journal of Structural Chemistry*, vol. 47, no. 2, pp. 258–266, 2006.
- [96] I. Abt, A. Caldwell, K. Kröniger, J. Liu, X. Liu, and B. Majorovits, “Neutron interactions as seen by a segmented germanium detector,” *The European Physical Journal A*, vol. 36, no. 2, pp. 139–149, 2008.
- [97] M. Braun, P. Hartmann, and C. Jana, “ ^{19}F and ^{31}P NMR spectroscopy of calcium apatites,” *Journal of Materials Science: Materials in Medicine*, vol. 6, no. 3, pp. 150–154, 1995.
- [98] “Laboratory Sample Preparation, United States Environmental Protection Agency,” July 2004.
- [99] S. Beckett, K. D. Rogers, and J. G. Clement, “Inter-Species Variation in Bone Mineral Behavior upon Heating^{*,†}: INTER-SPECIES VARIATION IN BONE MINERAL,” *Journal of Forensic Sciences*, vol. 56, pp. 571–579, May 2011.
- [100] M. Lebon, I. Reiche, J.-J. Bahain, C. Chadefaux, A.-M. Moigne, F. Fröhlich, F. Sémah, H. Schwarcz, and C. Falguères, “New parameters for the characterization of diagenetic alterations and heat-induced changes of fossil bone mineral using Fourier transform

- infrared spectrometry,” *Journal of Archaeological Science*, vol. 37, pp. 2265–2276, Sept. 2010.
- [101] C. Ooi, M. Hamdi, and S. Ramesh, “Properties of hydroxyapatite produced by annealing of bovine bone,” *Ceramics International*, vol. 33, pp. 1171–1177, Sept. 2007.
- [102] Y. Chen and X. Miao, “Thermal and chemical stability of fluorohydroxyapatite ceramics with different fluorine contents,” *Biomaterials*, vol. 26, no. 11, pp. 1205–1210, 2005.
- [103] S. Kannan, J. Rocha, S. Agathopoulos, and J. Ferreira, “Fluorine-substituted hydroxyapatite scaffolds hydrothermally grown from aragonitic cuttlefish bones,” *Acta Biomaterialia*, vol. 3, pp. 243–249, Mar. 2007.
- [104] D. J. White, W. D. Bowman, R. V. Faller, M. J. Mobley, R. A. Wolfgang, and J. P. Yesinowski, “¹⁹F MAS-NMR and solution chemical characterization of the reactions of fluoride with hydroxyapatite and powdered enamel,” *Acta Odontologica Scandinavica*, vol. 46, pp. 375–389, Jan. 1988.

- [105] M. Jiménez-Reyes and M. Solache-Ríos, “Sorptions behavior of fluoride ions from aqueous solutions by hydroxyapatite,” *Journal of Hazardous Materials*, vol. 180, pp. 297–302, Aug. 2010.
- [106] M. Lang, “Building a Birdcage Resonator for Magnetic Resonance Imaging Studies of CNS Disorders,” p. 43.
- [107] G. Carluccio and C. Collins, “BirdcageBuilder Mobile.”
- [108] C.-L. Chin, C. M. Collins, S. Li, B. J. Dardzinski, and M. B. Smith, “BirdcageBuilder: Design of specified-geometry birdcage coils with desired current pattern and resonant frequency,” *Concepts in Magnetic Resonance*, vol. 15, pp. 156–163, June 2002.
- [109] “Topspin.” Bruker Corporation, 2017.
- [110] “Structure analysis tools.” Software Department, Bruker Corporation, 2016.
- [111] J. Herzfeld and A. E. Berger, “Sideband intensities in NMR spectra of samples spinning at the magic angle,” *The Journal of Chemical Physics*, vol. 73, pp. 6021–6030, Dec. 1980.
- [112] S. G. Hyberts, S. A. Robson, and G. Wagner, “Exploring signal-to-noise ratio and sensitivity in non-uniformly sampled

- multi-dimensional NMR spectra,” *Journal of Biomolecular NMR*, vol. 55, pp. 167–178, Feb. 2013.
- [113] G. A. Eshak, H. M. Ahmed, and E. A. Abdel Gawad, “Gender determination from hand bones length and volume using multidetector computed tomography: A study in Egyptian people,” *Journal of Forensic and Legal Medicine*, vol. 18, pp. 246–252, Aug. 2011.
- [114] S. A. Steel, P. Swann, G. Langley, and C. M. Langton, “A phantom for evaluating bone mineral density of the hand by dual-energy x-ray absorptiometry,” *Physiological Measurement*, vol. 18, pp. 233–240, Aug. 1997.
- [115] H. Cho, P. Cappellaro, D. G. Cory, and C. Ramanathan, “Decay of highly correlated spin states in a dipolar-coupled solid: NMR study of Ca F_2 ,” *Physical Review B*, vol. 74, no. 22, p. 224434, 2006.
- [116] N. Gelman and R. F. Code, “Concentration dependence of ^{19}F nuclear magnetic resonance decay shapes and second moments in bone mineral,” p. 11, 1999.
- [117] H. Cho, T. D. Ladd, J. Baugh, D. G. Cory, and C. Ramanathan, “Multispin dynamics of the solid-state NMR free induction decay,” *Physical Review B*, vol. 72, no. 5, p. 054427, 2005.

- [118] L. B. Moran, J. K. Berkowitz, and J. P. Yesinowski, “F 19 and P 31 magic-angle spinning nuclear magnetic resonance of antimony (III)-doped fluorapatite phosphors: Dopant sites and spin diffusion,” *Physical Review B*, vol. 45, no. 10, p. 5347, 1992.
- [119] G. Cho, C.-N. Chau, and J. P. Yesinowski, “¹⁹F MAS NMR Investigation of Strontium Substitution Sites in Ca²⁺/Sr²⁺ Fluorapatite Solid Solutions,” *The Journal of Physical Chemistry C*, vol. 112, pp. 6165–6172, Apr. 2008.
- [120] F. M. McCubbin, H. E. Mason, H. Park, B. L. Phillips, J. B. Parise, H. Nekvasil, and D. H. Lindsley, “Synthesis and characterization of low-OH fluor-chlorapatite: A single-crystal XRD and NMR spectroscopic study,” *American Mineralogist*, vol. 93, pp. 210–216, Jan. 2008.
- [121] E. M. Haacke, S. Liu, S. Buch, W. Zheng, D. Wu, and Y. Ye, “Quantitative susceptibility mapping: Current status and future directions,” *Magnetic Resonance Imaging*, vol. 33, pp. 1–25, Jan. 2015.
- [122] A. Fatemi, E. M. Haacke, and M. D. Noseworthy, “Classification of calcium salts: Correlation of Magnetic Susceptibility With Susceptibility Weighted Imaging (SWI),”